

PHOTONIC CRYSTAL BASED OPTICAL DEVICES

by

Tao Liu

---

A Dissertation Submitted to the Faculty of the  
COLLEGE OF OPTICAL SCIENCES

In Partial Fulfillment of the Requirements  
For the Degree of

DOCTOR OF PHILOSOPHY

In the Graduate College

THE UNIVERSITY OF ARIZONA

2005

THE UNIVERSITY OF ARIZONA  
GRADUATE COLLEGE

As members of the Dissertation Committee, we certify that we have read the dissertation prepared by Tao Liu entitled Photonic Crystal Based Optical Devices and recommend that it be accepted as fulfilling the dissertation requirement for the Degree of Doctor of Philosophy

\_\_\_\_\_  
Masud Mansuripur Date: 08/26/2005

\_\_\_\_\_  
Mahmoud Fallahi Date: 08/26/2005

\_\_\_\_\_  
Alan Kost Date: 08/26/2005

Final approval and acceptance of this dissertation is contingent upon the candidate's submission of the final copies of the dissertation to the Graduate College.

I hereby certify that I have read this dissertation prepared under my direction and recommend that it be accepted as fulfilling the dissertation requirement.

\_\_\_\_\_  
Dissertation Director: Masud Mansuripur Date: 08/26/2005

## STATEMENT BY AUTHOR

This dissertation has been submitted in partial fulfillment of requirements for an advanced degree at the University of Arizona and is deposited in the University Library to be made available to borrowers under rules of the Library.

Brief quotations from this dissertation are allowable without special permission, provided that accurate acknowledgment of source is made. Requests for permission for extended quotation from or reproduction of this manuscript in whole or in part may be granted by the head of the major department or the Dean of the Graduate College when in his or her judgment the proposed use of the material is in the interests of scholarship. In all other instances, however, permission must be obtained from the author.

TYPE NAME HERE: Tao Liu

## ACKNOWLEDGEMENT

I would like to express my gratitude to my supervisor, Prof. Masud Mansuripur, for his support, patience, and encouragement throughout my graduate studies. His technical and editorial advice was essential to the completion of this dissertation and has taught me innumerable lessons and insights on the workings of academic research in general.

My thanks also go to the members of my major committee, Prof. Mahmoud Fallahi and Prof. Alan Kost for reading previous drafts of this dissertation and providing many valuable comments that improved it. Especially I am highly indebted to Prof. Mahmoud Fallahi for his supervision in the area of microfabrication.

I am also grateful to Prof. Jerome V. Moloney and Dr. Aramis Zakharian for allowing us to use their MX3D software and many insightful discussions. My thanks go to Dr. Chubin Peng, Mr. Kevin J. Erwin, and Mr. Warren L. Bletscher for their help during building up the blue laser writer system. I would also like to acknowledge with much appreciation the kind help from Dr. Robert Bedford for teaching me how to use the electron-beam lithography system and the ECR-RIE etching system in the cleanroom.

Last, but not least, I would like to thank my wife Wen for her understanding and love during the past few years. Her support and encouragement was in the end what made this dissertation possible.

## TABLE OF CONTENTS

LIST OF ILLUSTRATIONS-----	7
LIST OF TABLES-----	13
ABSTRACT-----	14
1. INTRODUCTION-----	15
1.1 Background-----	15
1.2 Outline of the Dissertation-----	21
2. NUMERICAL METHODS-----	24
2.1 Basic Equations-----	24
2.2 Frequency-Domain Method-----	25
2.3 Finite-Difference Time-Domain Method-----	26
3. MULTIMODE INTERFERENCE-BASED PHOTONIC CRYSTAL WAVEGUIDE POWER SPLITTER-----	30
3.1 Introduction-----	30
3.2 Power Splitter Based on MMI Effect and Photonic Crystals-----	31
3.3 An Example of Mach-Zehnder Interferometer Based on MMI Power Splitter and Combiner-----	40
3.4 Conclusion-----	44
4. DESIGN OF A COMPACT PHOTONIC-CRYSTAL-BASED POLARIZING BEAM SPLITTER-----	45
4.1 Introduction-----	45
4.2 Design and Analysis-----	47
4.3 Conclusion-----	54
5. AN INTERSECTION OF NON-IDENTICAL OPTICAL WAVEGUIDES BASED ON PHOTONIC CRYSTALS-----	55
5.1 Introduction-----	55
5.2 Design and Analysis-----	56
5.3 Conclusion-----	65

## TABLE OF CONTENTS-*Continued*

6. DESIGN OF PHOTONIC CRYSTAL COUPLED-RESONATOR- OPTICAL-WAVEGUIDES WITH SINGLE MODE PROPAGATION IN THE BANDGAP-----	66
6.1 Introduction-----	66
6.2 Design and Analysis-----	67
6.3 Conclusion-----	72
7. FABRICATING TWO-DIMENSIONAL PHOTONIC CRYSTALS WITH EMBEDDED DEFECTS USING BLUE-LASER-WRITER AND OPTICAL HOLOGRAPHY-----	73
7.1 Introduction-----	73
7.2 Blue-Laser-Writer Optical System-----	75
7.3 Optical Holography System-----	82
7.4 Fabricating Two-Dimensional Photonic Crystals with Defects -----	85
7.5 Measurement -----	89
7.6 Discussion and Conclusion-----	93
8. TRANSMISSION MEASUREMENT ON PHOTONIC CRYSTAL WAVEGUIDES FABRICATED ON InP BASED SUBSTRATES-----	95
9. CONCLUDING REMARKS AND FUTURE PERSPECTIVES-----	100
REFERENCES-----	103

## LIST OF ILLUSTRATIONS

- Figure 1.1 Schematic of three kinds of photonic crystals: one-dimensional, two-dimensional, and three-dimensional photonic crystals. ----- 17
- Figure 1.2 Two-dimensional photonic crystal slab structure: light can be confined with photonic bandgap effect in the plane of periodicity, and with index contrast in the vertical direction. ----- 18
- Figure 1.3 The relationship between the photonic bandgap size and the index contrast for (a) a triangular lattice of air holes with  $r = 0.45a$ , and (b) a square lattice of air holes with  $r = 0.50a$ .  $r$  is the radius of the air holes and  $a$  is the period of the lattice.  $\Delta n$  is the index contrast. Normalized unit  $c/a$  is used for the frequency with  $c$  as the speed of light in free space. The index of the host material is chosen to be 3.4. ----- 19
- Figure 3.1 Projected band structures of a square lattice of infinite columns ( $\epsilon_{rod} = 11.56$ ) in air ( $\epsilon = 1$ ) with (a) one missing row and (b) five missing rows of dielectric columns.  $r/a = 0.18$  where  $r$ : radius of rods  $a$ : pitch. Both figures are for the TM mode, whose electric field is parallel to the infinite dielectric columns. The insets show the corresponding waveguide structures. ----- 33
- Figure 3.2 (a) Schematic diagram of a junction connecting a single-mode waveguide and a multimode waveguide. (b) Distribution of Poynting vector component along the waveguide direction at  $\lambda_0 = 1.55\mu\text{m}$ . (c) Simulated electric field amplitude distribution at  $\lambda_0 = 1.55\mu\text{m}$ . ----- 36
- Figure 3.3 (a) Simulated waveguide power splitter. (b) Magnified view of the vicinity of the splitter section. (c) Steady state electric field distribution at  $\lambda_0 = 1.55\mu\text{m}$  in the vicinity of the splitter section. -----37
- Figure 3.4 Transmission efficiency from the single input waveguide into the two output waveguides and the reflection from the multimode junction. ----- 37
- Figure 3.5 (a) Schematic diagram of the compact waveguide power splitter connected with two sharp bends. (b) Simulated electric field distribution at  $\lambda_0 = 1.55\mu\text{m}$ . ----- 39

## LIST OF ILLUSTRATIONS-*Continued*

- Figure 3.6 (a) Schematic diagram of a Mach-Zehnder interferometer with symmetric arms and the simulated electric field distribution. 3 columns indicated by A and 4 columns indicated by B are moved upward by half period. (b) A Mach-Zehnder interferometer with asymmetric arms and the simulated electric field distribution at  $\lambda_0 = 1.55\mu\text{m}$ . The extra columns indicated by C are located in the central region of the right arm and have the size of  $0.1a$  compared to  $0.18a$  for regular columns. The distance between 2 neighboring extra columns is  $2a$ .  $a$  is the period of the photonic crystal. (c) Mach-Zehnder interferometer with symmetric arms, and the corresponding simulated  $E$ -field distribution. There are five identical extra columns in each arm. Note the high level of transmission. The simulated  $E$ -field distribution is obtained at  $\lambda_0 = 1.55\mu\text{m}$  in all these cases. ----- 41
- Figure 4.1 Diagram of the proposed PBS based on a PC directional coupler. The effective refractive index of the host material is 3.32; the period of the triangular lattice of air holes is  $a=0.457\mu\text{m}$ ; the radius of the lattice holes is  $r_0=0.147\mu\text{m}$ , while the radius of the smaller holes that separate the two guides in the coupler region is  $r_l=0.118\mu\text{m}$ . The lengths of the input guide and the directional coupler are  $15a$  and  $53a$ , respectively. The top waveguide is referred to as the direct channel, while the bottom guide is called the adjacent channel. Also shown are three line detectors used in the FDTD simulations: 1 to monitor the power input into the directional coupler, 2 to monitor the power in the direct channel, and 3 to monitor the power in the adjacent channel. --48
- Figure 4.2 Computed transmission efficiency for the direct channel and the adjacent channel for (a) TE light and (b) TM light. ----- 51
- Figure 4.3 Simulated Poynting vector distribution along the guide direction for (a) TE light and (b) TM light in the structure shown in Fig.4.1. The optical wavelength is  $1.554\mu\text{m}$ . ----- 52
- Figure 5.1 (a) Schematic of an intersection based on a square lattice of infinite columns ( $\epsilon_{rod} = 11.56$ ) in air ( $\epsilon = 1$ ).  $r/a = 0.18$  where  $r$  is radius of the columns and  $a$  is the pitch. The defect columns of the vertical CROW are completely removed, while the defect columns of the horizontal CROW have the reduced radius of  $0.1a$ . (b) Projected band structures of the two CROWs for the TM mode, whose electric field is parallel to the dielectric columns. -----58

## LIST OF ILLUSTRATIONS-*Continued*

- Figure 5.2 Schematic of an alternate intersection with a microcavity at the center based on a square lattice of infinite columns. -----59
- Figure 5.3 Schematic of two structures used in transmission efficiency calculations. (a) is for the vertical CROW and (b) for the horizontal CROW as shown in Fig.1(a). The total length and width of the structures are  $200a$  and  $16a$ , with the intersection  $80a$  away from the left end. One monitor is placed  $41a$  away from the left end, while the other one is  $9a$  to the right of the intersection ( $a$  is the period of the square lattice). Both monitors are located at the center of the cavities. ----- 61
- Figure 5.4 Transmission efficiency of the light passing through the intersection for the vertical waveguide (a) and horizontal waveguide (b). Results from different pulses are plotted with different line shapes. Pulse centers are also given. --62
- Figure 5.5 Simulated  $E$ -field distribution of (a) vertical arm at  $1.31\mu\text{m}$ , and (b) horizontal arm at  $1.55\mu\text{m}$  corresponding to the structure in Fig. 5.1(a). For the vertical propagation, light is incident from the bottom; for the horizontal propagation, light is incident from the left. -----64
- Figure 6.1 (a) A CROW along the  $\Gamma$ -K direction of a two-dimensional triangular lattice photonic crystal of air holes in silicon with refractive index of 3.4. (b) One unit cell and the mode profiles of the even and odd TE modes of the CROW. (c) Dispersion diagram of the CROW in the photonic bandgap.  $r/a = 0.32$  where  $r$ : radius of air holes  $a$ : pitch. The magnetic fields for both TE modes are normal to the plane of periodicity.  $d$  is the pitch of the CROW. In this case,  $d = 2a$ . ----- 69
- Figure 6.2 (a) Shape of the anisotropic defect hole.  $W$  is the width of the rectangle and the diameter of the two semi-circles.  $L$  is the length of the middle rectangle. (b) The even mode profile for the modified CROW with  $w = 0.3a$  and  $L = 0.6a$ . All the other holes have the radius of  $0.32a$ . (c) The odd TE mode for several sizes of the defect. (d) The even TE mode for several sizes of the defect. The magnetic fields for both TE modes are normal to the plane of periodicity.  $d$  is the pitch of the CROW. In this case,  $d = 2a$ . ----- 71

## LIST OF ILLUSTRATIONS-*Continued*

- Figure 7.1 Picture of the entire blue-laser-writer optical system. -----77
- Figure 7.2 Schematic and a picture of the interferometers setup. A HeNe laser is used here. There are two interferometers: one for X-axis, the other for Y-axis. --78
- Figure 7.3 Schematic and a picture of the auto-focus and writing setup. A blue laser is used for writing and a red laser is used for auto-focus. ----- 79
- Figure 7.4 Schematic of the control system for the blue-laser-writer optical system. Picomotors for X, Y, and Z directions are connected to the parallel port through a network controller; Detectors 1, 2, and 3 for the interferometers, and quadruple detector for the auto-focus part are connected to a data acquisition (DAQ) board and then to the computer; the blue laser for the writing is connected to the computer through a serial part. -----80
- Figure 7.5 Pictures of several straight lines written into photoresist by the blue laser writer optical system. Pictures were taken after development in 351. The output power from the blue laser is 1.0mW, and the actual power on the sample for the writing is 50nW. The numerical aperture (NA) used here is 0.6. The length of each line is 50 $\mu$ m. The writing is done point-by-point and the point spacing is 1 $\mu$ m. With the exposure time at each point increasing from 10ms to 500ms, the linewidth increases as well. -----81
- Figure 7.6 Schematic of the two-beam interferometric optical holography. The laser emits two wavelengths: 325nm and 441.6nm. Two filters in front of the laser can be used to select the desired wavelength. 441.6nm is used in our experiment because the optics is not transparent at 325nm. The direction of polarization of the laser beam is normal to the plane. Objective lens in the spatial filter: X60/0.85; Pinhole in the spatial filter: 5 $\mu$ m; Collimator: F5/250mm. The iris after the collimator selects the central uniform part of the collimated beam. Another metallic mirror and the sample holder are mounted on the same rotational stage with 90 degrees. ----- 83

## LIST OF ILLUSTRATIONS-*Continued*

- Figure 7.7 Pictures of photonic crystals fabricated by optical holography: (a) pictures taken under an optical microscope for overall view; (b) Scanning Electron Microscope (SEM) micrographs for two different exposures. The period of the square lattice is  $1.0\mu\text{m}$ . The photonic crystal patterns are in the photoresist after development. ----- 84
- Figure 7.8 Schematic of the fabrication procedures for creating defects into photonic crystals. PR: photoresist; BLW: blue laser writer. ----- 86
- Figure 7.9 SEM micrographs of the PCs with defects in Cr. These figures are corresponding to Fig.7.8(7). The  $\text{SiO}_2$  layer in the defect regions is clearly visible. ----- 88
- Figure 7.10 SEM micrographs of the PCs with defects in InP. These figures are corresponding to Fig.7.8(8). ----- 88
- Figure 7.11 Cross sectional view of the PCs in InP after dry etching for (a) 30 min; (b) 60 min. These figures are corresponding to Fig.7.8(8). ----- 88
- Figure 7.12 Schematic of the InP-based heterostructure for the fabrication of the photonic crystals with defects for the measurement. ----- 90
- Figure 7.13 Measurement setup for the fabricated photonic crystal device. ---- 91
- Figure 7.14 Beam splitting at  $\lambda=1540\text{nm}$  for TE polarization. Top: picture of the fabricated beam splitter (taken with an optical microscope); Bottom: SEM micrograph of the splitter region; Right: signals detected by an IR camera placed at the output end of the splitter for in-plane view. ----- 91
- Figure 8.1 Fabrication procedures of photonic crystal optical components: (1) Spin-coat E-beam resist PMMA on top of the sample; (2) Define photonic crystal patterns into PMMA with E-beam lithography, then remove the exposed area; (3) The patterns are transferred from PMMA to  $\text{SiO}_2$  with ECR-RIE etching and the residual PMMA is removed; (4) The patterns are transferred from

## LIST OF ILLUSTRATIONS-*Continued*

SiO<sub>2</sub> to the underlying wafer with ECR-RIE etching and the residual SiO<sub>2</sub> hard mask is removed. -----97

Figure 8.2 (a) SEM image of the PC waveguide region. (b) Magnified view of the right PC interface with the ridge waveguide. (c) Magnified view of the left PC interface with the ridge waveguide. (d) Cross-sectional view of the ridge. (e) Cross-sectional view of the PC waveguide. ----- 98

Figure 8.3 (a) Photograph of the measurement setup: two lensed fibers on either side of the sample are used to couple the light in and out of the waveguides. (b) Magnified view of the S-bend ridge waveguide without the PC section. (c) Magnified view of the S-bend structure with an embedded PC device. --99

Figure 8.4 Preliminary measurement result showing the insertion loss of the PC waveguide calibrated against the blank ridge waveguide. The minimum loss is ~-5 dB around  $\lambda = 1540$  nm. -----99

## LIST OF TABLES

Table 3.1	Mode Properties of the Multimode Waveguide in Fig.3.1(b) at the Specified Frequency. -----	34
-----------	--	----

## **ABSTRACT**

Photonic crystals have the capability to control electromagnetic waves due to the existence of photonic bandgap. The devices based on photonic crystal structures usually have the advantage of substantial size reduction compared to their conventional counterparts, which may lead to miniaturization and large-scale integration of optical and opto-electronic devices.

In this dissertation, several novel optical devices based on photonic crystals are designed and analyzed, including a compact power splitter, a compact polarizing beam splitter, an optical intersection of nonidentical optical waveguides, and a single mode coupled resonator optical waveguide. The simulation results show superior advantages compared to their conventional counterparts. In addition, a new fabrication method based on combining a custom-built blue laser writer and the technique of optical holography is developed for the purpose of mass production of useful photonic crystal devices.

# CHAPTER 1

## INTRODUCTION

### 1.1 Background

The idea of photonic crystal (PCs) or photonic band gap (PBG) materials was first suggested in 1987 [1]. For periodic composite media made by appropriated choices of geometric and physical parameters, complete band gaps could be created. In the frequency range of the band gaps, electromagnetic waves are forbidden to propagate in any direction and with any polarization [2].

The concept of PBG is analogous to band gaps in semiconductors. A semiconductor crystal is a periodic arrangement of atoms or molecules that presents a periodic potential to an electron propagating through it. Due to Bragg-like diffraction from the atoms, energy gaps might be introduced into the band structure of the crystal. In this energy gap, electrons are not allowed to exist. In a similar manner, a photonic crystal is a periodic arrangement of macroscopic dielectric media instead of atoms and the period of the crystal is on the order of the light wavelength. If the difference between the dielectric constants of the materials forming the crystal is large enough, photonic band gaps could appear, which allows us to control the light propagation on the order of light wavelength.

In terms of dimensionality, photonic crystals can be classified into three categories: one-dimensional, two-dimensional, and three-dimensional photonic crystals, as shown in

Fig 1.1. One-dimensional photonic crystals are periodic arrangement of dielectric media in only one dimension, which are just like conventional multilayer structures. For the one-dimensional system, photonic band gaps might exist for normally incident light. Similarly, two-dimensional photonic crystals have periodicity in two dimensions and light could be confined only in these two dimensions with photonic band gap effect. Three-dimensional photonic crystals have periodicity in three dimensions and light could be confined in all three dimensions with photonic band gap effect.

In order to realize functional PC devices like optical waveguides and microcavities, various defect structures have to be incorporated into the otherwise periodic structures [2]-[12]. However, due to the extreme difficulty to make the required defects in three-dimensional PCs, most researchers have been focusing on two-dimensional PCs on slab platforms. In this way, light can be controlled in all three dimensions with photonic band gap effect for in-plane confinement and total internal reflection for the vertical confinement because of the index contrast. A schematic of this kind of slab is shown in Fig.1.2.

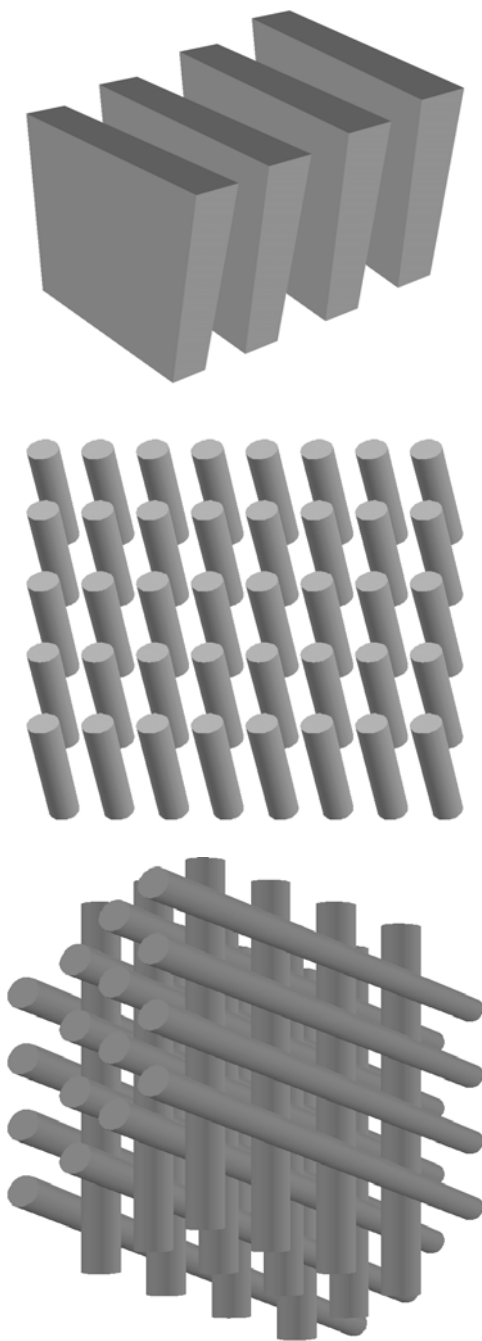


Fig 1.1 Schematic of three kinds of photonic crystals: one-dimensional, two-dimensional, and three-dimensional photonic crystals.

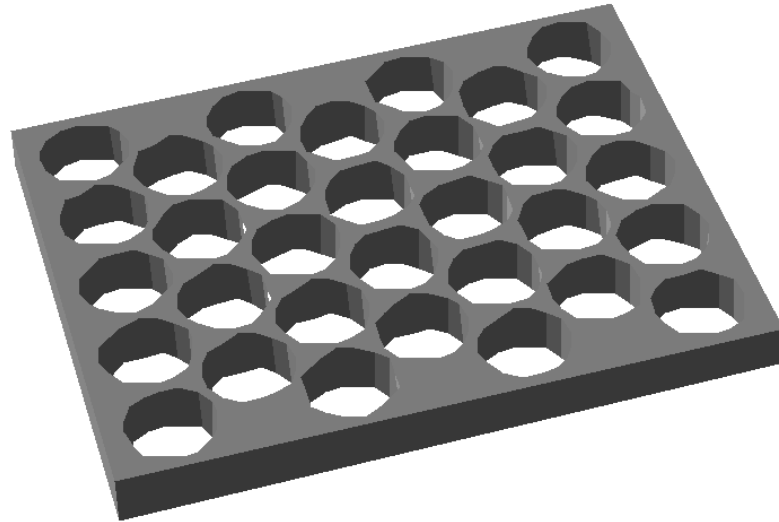


Fig. 1.2 Two-dimensional photonic crystal slab structure: light can be confined with photonic bandgap effect in the plane of periodicity, and with index contrast in the vertical direction.

For the host materials, most of researchers work on semiconductors, including Si, InP, GaAs, etc. The reason is that these materials have very high indices around 3.5. Together with other suitably chosen structural parameters, these materials can give large photonic bandgaps [2]. In order to show the importance of the index of the host material for photonic crystals, we computed the dependence of the bandgap size on the index contrast in Fig. 1.3. The index contrast is defined as the refractive index difference between the host material and the periodic element. Two widely studied lattices are used here: a triangular lattice in Fig. 1.3(a) and a square lattice in Fig. 1.3(b). It can be seen that the bandgap gradually decreases until it closes completely at a threshold index contrast.

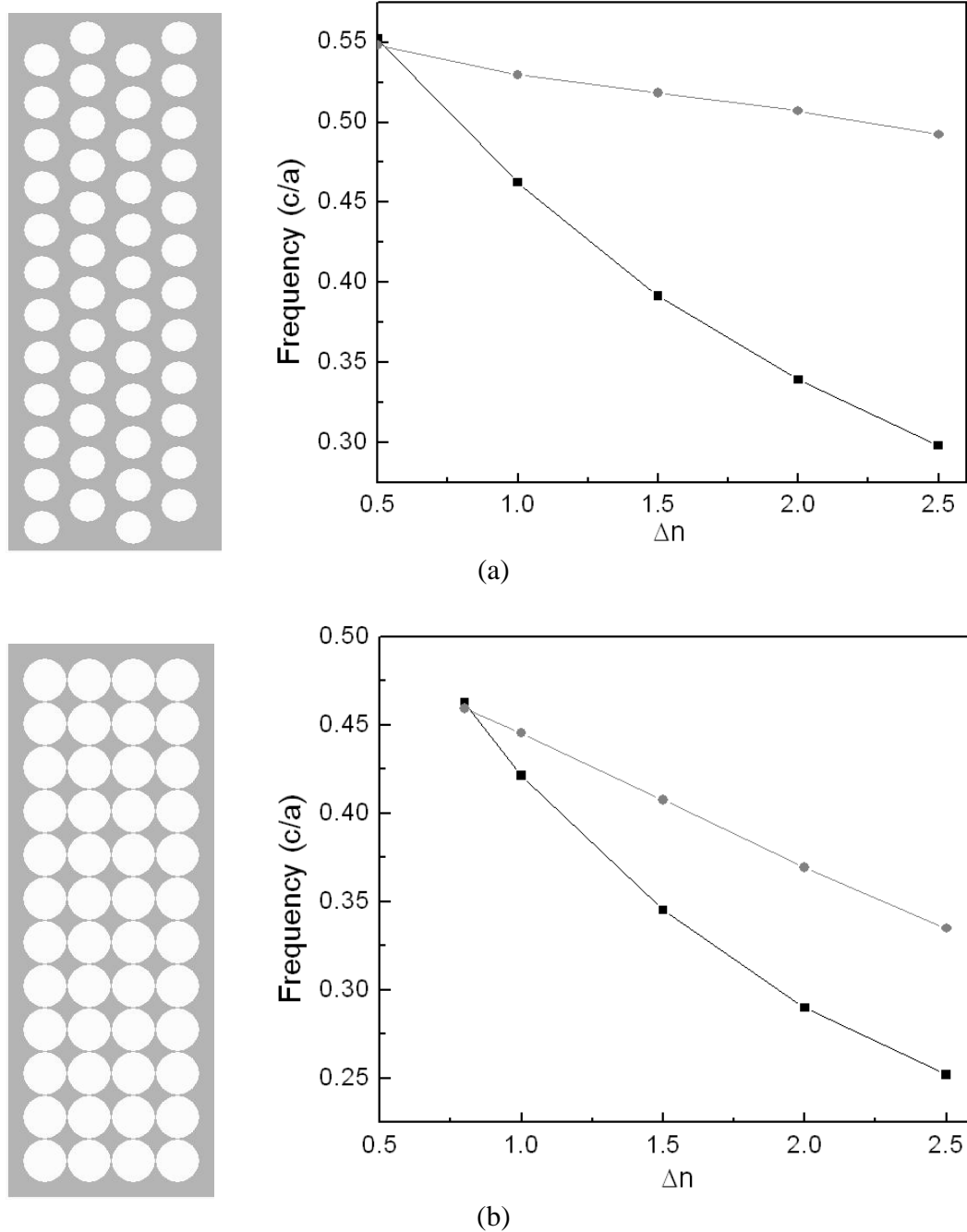


Fig. 1.3 The relationship between the photonic bandgap size and the index contrast for (a) a triangular lattice of air holes with  $r = 0.45a$ , and (b) a square lattice of air holes with  $r = 0.50a$ .  $r$  is the radius of the air holes and  $a$  is the period of the lattice.  $\Delta n$  is the index contrast. Normalized unit  $c/a$  is used for the frequency with  $c$  as the speed of light in free space. The index of the host material is chosen to be 3.4.

Photonic crystals hold the promise for the construction and integration of optical components in a very compact manner and are viewed as the basis for constructing very large-scale optical integrated circuits. One reason is that photonic crystals can be used to build very sharp bends that cannot be realized with conventional optical waveguides with low loss [5]. For conventional optical waveguide bends, the radii of the bends have to be very large otherwise much of the light would be lost during the transmission due to the fact that the total internal reflection cannot be satisfied. This drawback of the conventional optical waveguides limits the integration density of optical integrated circuits. Fortunately, this drawback might be overcome by photonic crystals. On the other hand, with photonic crystals light can be controlled spatially on the order of optical wavelength and optical devices based on photonic crystals usually have the advantage of dramatic size reduction compared to their conventional counterparts, which makes them ideal for constructing integrated circuits with very large density. In this thesis, four new photonic crystal based optical devices, including a multimode interference based power splitter, a compact polarizing beam splitter, an optical intersection, and a single mode photonic crystal coupled-resonator-optical-waveguide (CROW), are designed and analyzed. The size reduction can be clearly seen.

Fabrication is another important issue for applications of photonic crystals. Currently, electron beam lithography is a commonly used technique for fabricating 2D PCs with high degree of accuracy and design flexibility [13]-[16]. However, direct-write E-beam lithography is a slow and expensive process, which makes it inappropriate for the mass

production of large integrated optical circuits. By comparison, optical holography is an ideal candidate for making PCs with high throughput on a large area [17]. But optical holography itself can only produce PCs without any defect structures that are necessary for realizing functional optical components. For this reason, we develop a new method to produce PCs with controlled defects by combining a custom-built blue-laser-writer and the technique of optical holography. We believe that, with this method, various defects can be fabricated to produce different functional PCs at low cost and large volume.

## 1.2 Outline of the Dissertation

This dissertation is organized as followed.

In Chapter 2, two different numerical methods used to design the photonic crystals are discussed. The first solves Maxwell's equations in the frequency domain, while the second solves the equations in the time domain. These two methods reveal different information about photonic crystals. The frequency-domain method gives the frequency, polarization, symmetry, and field distribution of all the eigenmodes, while the time-domain method can be used to determine the temporal behavior of the photonic crystal devices. In this thesis, the frequency-domain method is used to compute the band structure of different photonic crystal structures, while the time-domain method is used to evaluate the performance of the designed devices.

In Chapter 3, a compact power splitter based on multimode interference effect in photonic crystal waveguides is designed and analyzed. The device size reduction

compared to the conventional MMI power splitter can be attributed to the large dispersion of the photonic crystal waveguides. We also show an example of the application of the multimode mode interference effect in photonic crystals to design a compact Mach-Zehnder interferometer.

In Chapter 4, a compact polarizing beam splitter based on a photonic crystal directional coupler with a triangular lattice of air holes is designed and simulated. In the employed photonic crystal structure, TE light is confined with the photonic bandgap effect, while TM light is guided through an index-like effect. Due to the different guiding mechanisms, TM and TE light have strikingly different beat lengths, which is utilized to separate the two polarizations in a directional coupler no longer than  $24.2\mu\text{m}$ . The extinction ratios are found to be around 20dB for both TE and TM polarized light.

In Chapter 5, an intersection based on photonic crystal coupled resonator optical waveguides is proposed and analyzed. The two waveguides are designed to have different transmission bands without overlap, which enables light in the two corresponding bands to propagate through the intersection with no cross-talk and with excellent transmission. This design is for the purpose of accommodating the wide transmission band in the current optical communication systems.

In Chapter 6, we presented a way to design a single mode  $\Gamma$ -K direction CROW in a triangular lattice photonic crystal of air holes in a dielectric. It is shown that insertion of

an extra anisotropic hole along a specific direction in the cavity can lead to single even mode transmission in the whole bandgap region, which is important for many practical applications.

In Chapter 7, we demonstrate an approach of relatively rapid fabrication of two-dimensional photonic crystals with embedded defects by combining a custom-built blue-laser-writer and the technique of optical holography. The blue laser writer is used to define various defect patterns first, and then the optical holography is used to create two-dimensional photonic crystals on the samples with the pre-defined defects. Finally the photonic crystal patterns are transferred into the InP substrates by ECR-RIE etching.

In Chapter 8, Electron-beam lithography and ECR-RIE dry etching are used to make photonic crystal structures with much flexibility. Complete processing procedures are developed. Some preliminary measurement results for the coupling between conventional ridge waveguides and photonic crystal waveguides are also presented.

## CHAPTER 2

### NUMERICAL METHODS

#### 2.1 Basic Equations

All of macroscopic electromagnetism, including the propagation of light in photonic crystals, is governed by the following four Maxwell equations:

$$\nabla \cdot \vec{B} = 0 \quad (2.1)$$

$$\nabla \cdot \vec{D} = 4\pi\rho \quad (2.2)$$

$$\nabla \times \vec{E} + \frac{1}{c} \frac{\partial \vec{B}}{\partial t} = 0 \quad (2.3)$$

$$\nabla \times \vec{H} - \frac{1}{c} \frac{\partial \vec{D}}{\partial t} = \frac{4\pi}{c} \vec{J} \quad (2.4)$$

where  $E$  and  $H$  are the macroscopic electric and magnetic fields,  $D$  and  $B$  are the displacement and magnetic field induction fields, and  $\rho$  and  $J$  are the free charges and currents. In the absence of free charges and currents,  $\rho$  and  $J$  can be set to be zero.

The constitutive equations (2.5) relate  $D$  to  $E$  and  $B$  to  $H$ .

$$D_i = \sum_j \varepsilon_{ij} E_j + \sum_{j,k} \chi_{ijk} E_j E_k + O(E^3) \quad (2.5)$$

In this thesis, we assume that the field strengths are small enough so that we are in the linear regime, therefore  $\chi$  and all higher terms can be ignored. We mainly deal with isotropic media, which means that  $\mathbf{E}$  and  $\mathbf{D}$  are related by a scalar dielectric constant  $\epsilon$ . We also assume that the dielectric constant  $\epsilon$  is frequency independent. Finally, in the frequency of interest, the materials are considered low-loss; therefore the dielectric constant  $\epsilon$  can be treated as a real constant. For most dielectric materials of interest, the magnetic permeability is very close to unity and  $\mathbf{B}$  can be set equal to  $\mathbf{H}$ .

## 2.2 Frequency-Domain Method

In the frequency-domain method, we are trying to solve the field distributions of the steady state from the Maxwell equations (2.1) to (2.4). The fields are expanded into a set of harmonic modes that have the following temporal characteristics:

$$\vec{H}(\vec{r}, t) = \vec{H}(\vec{r})e^{i\omega t} \quad (2.6)$$

$$\vec{E}(\vec{r}, t) = \vec{E}(\vec{r})e^{i\omega t} \quad (2.7)$$

After substituting the above equations (2.6) to (2.7) into the Maxwell equations (2.1) to (2.4), we can obtain the following equation for the magnetic field  $\mathbf{H}$ :

$$\nabla \times \left( \frac{1}{\epsilon(\vec{r})} \nabla \times \vec{H}(\vec{r}) \right) = \left( \frac{\omega}{c} \right)^2 \vec{H}(\vec{r}) \quad (2.8)$$

Equation (2.8) defines an eigenvalue problem and can be solved by a variational approach. After the magnetic field  $\vec{H}$  is found, the electric field can be obtained by the following relation:

$$\vec{E}(\vec{r}) = \left( \frac{-ic}{\omega\epsilon(\vec{r})} \right) \nabla \times \vec{H}(\vec{r}) \quad (2.9)$$

In this thesis, most of the band structure calculations are done with a free software MPB-BAND developed by the Physics Department of Massachusetts Institute of Technology (MIT) [18]. MPB-BAND solves Maxwell equations in frequency-domain method and gives the band structures of photonic crystals.

### 2.3 Finite-Difference Time-Domain Method

Finite-difference time-domain method (FDTD) has been widely used in the area of computational electrodynamics to analyze the interactions between electromagnetic waves and complex dielectric or metallic structures [19]. In the general procedures, finite differences are used to approximate Maxwell equations in real space and appropriate boundary conditions are imposed in order to simulate finite or infinite structures. Then the response of the structure to the electromagnetic waves in time domain can be obtained by time-marching the fields.

The Maxwell curl equations are discretized on the Yee's lattice. The fields variables are defined on a rectangular grid. Electric and magnetic fields are temporarily separated by one-half time step. Also, the electric and magnetic fields are spatially interlaced by half a grid cell. Based on this scheme, finite differences in both time and space are used to approximate the Maxwell equations on each grid point.

In order to compute the field at any given grid point on a Yee's lattice, the field values at every adjacent grid point on the grid have to be known first. But with a finite computational domain, the field values from grid points outside the domain are not available. Therefore, field values on the boundaries have to be updated by using appropriate boundary conditions.

### 2.3.1 Periodic Boundary Condition for Band Structure Calculation

In addition to frequency-domain method, finite-difference time-domain method can also be used to obtain the band structures of photonic crystals. The computational domain is chosen to be a unit cell of the infinite photonic crystal. The fields at nodes outside the computational domain (unit cell) are related to those fields inside by the periodic boundary condition (Bloch's theorem):

$$\vec{H}(\vec{r} + \vec{a}, t) = \vec{H}(\vec{r}, t)e^{i\vec{k} \cdot \vec{a}} \quad (2.10)$$

$$\vec{E}(\vec{r} + \vec{a}, t) = \vec{E}(\vec{r}, t)e^{i\vec{k} \cdot \vec{a}} \quad (2.11)$$

where  $r$  is the vector of the node in the computational domain,  $a$  is the lattice vector, and  $k$  is the wavevector.

Modes in the computational unit cell can be excited by using point dipole sources or an initial field with random distribution. The initial excitation has Gaussian profile in frequency space with suitable oscillation period and width to cover the frequency range of interest. If dipole point sources are used, the positions of the sources have to be carefully chosen such that they are away from all symmetry planes and therefore all the modes with different symmetries can be excited. (e.g. odd source distribution cannot excite even modes, and vice versa.) After the initial excitation, fields in the computational domain will oscillate in a steady state that is a linear combination of all the eigenstates with the same wavevector  $k$ . Field amplitudes in time domain recorded at a chosen point (away from symmetry planes also) are Fourier transformed to find the discrete peaks in the resulting spectrum that are corresponding to the frequencies of all the eigenstates. Similar calculations are then repeated for all the wavevectors and finally the band structure for the infinite photonic crystal can be obtained. The positions for the dipole sources, the oscillation period, and the width of the Gaussian profile can be carefully chosen to excite only those modes of interest.

### 2.3.2 Absorbing Boundary Conditions for Modeling Unbounded Geometries

Berenger's Perfectly Matched Layer (PML) boundary condition is used in this thesis. PML is based on applying artificial absorbers on the boundaries that are designed to be

impedance-matched with free space and the reflection can be completely cancelled regardless of the incident angle.

In this thesis, the FDTD code used for modeling the photonic crystal devices are developed by the Arizona Center of Mathematical Sciences (ACMS).

# CHAPTER 3

## MULTIMODE INTERFERENCE-BASED PHOTONIC CRYSTAL WAVEGUIDE POWER SPLITTER

### 3.1 Introduction

Photonic crystals have gained worldwide interest in the past few years. They have the capability to control electromagnetic waves due to the existence of photonic bandgap [2]. Various types of optoelectronic devices have been presented [3], [4], [20], [21]. The devices based on photonic crystal structures usually have the advantage of substantial size reduction compared to their conventional counterparts [5]-[7], [20], [22], [23]. This unique capability may lead to miniaturization and large-scale integration of optical and optoelectronic devices. Optical power splitter is an important component in integrated optical circuits. Photonic crystal optical power splitters based on T-junction or Y-junction have been analyzed [8], [24]. In this paper we present a new design of power splitter based on multimode-interference (MMI) effect in photonic crystal waveguides.

MMI devices are important components for photonic and optoelectronic integrated circuits due to their simple structure, low polarization dependence, low loss, and large optical bandwidth. These structures provide power splitting-combining and have found many applications in 3dB couplers, Mach-Zehnder interferometers (MZI), ring lasers, and optical switches [25]-[27].

The operation of multimode interference (MMI) devices is based on the self-imaging principle, which is a property of multimode waveguides by which an input field profile is reproduced in single or multiple copies at regular intervals along the propagation direction of the waveguide. Due to their large dispersion, MMI devices based on photonic crystal waveguides have the potential to be much smaller than conventional MMI devices.

The simplest MMI device is a  $1 \times 2$  waveguide splitter/combiner, which needs just two symmetric modes. In this paper the emphasis will be on design and analysis of a  $1 \times 2$  waveguide splitter based on MMI effect in photonic crystal structures. The power splitter presented in this paper works for TM mode only because the photonic crystal structures used here have bandgap for TM mode only. This idea can be easily extended to more complex photonic crystal structures such as  $N \times M$  MMI couplers, where  $N$  and  $M$  are the number of input and output waveguides respectively.

### 3.2 Power Splitter Based on MMI Effect and Photonic Crystals

The basic components for the  $1 \times 2$  waveguide splitter that we investigate are two types of straight 2-D waveguides, obtained by removing either one row or five rows from a square lattice of infinitely long dielectric columns in air [2]. The columns have dielectric constant  $\epsilon_{\text{rod}} = 11.56$  and radius  $r = 0.18a$ , where  $a$  is the column-to-column pitch. The MIT Photonic-Bands code [18] is used to calculate the projected band structure of the photonic crystal waveguides shown as the insets in Fig.3.1. With the

selected parameters, the 2-D square lattice has a band gap for TM mode in the spectral range  $0.30 \leq a/\lambda_0 \leq 0.44$ ,  $\lambda_0$  being the optical wavelength in free space.

Figure 3.1(a) shows the projected band structure of a photonic crystal with a single linear defect (one missing row of dielectric columns). The gray regions are zones in which the dispersion curves of extended modes of the infinitely long square lattice lie, in the absence of any defect. The dispersion curve of the guiding mode in this linear defect waveguide is clearly seen in the photonic bandgap region. There is only one guiding mode in the bandgap region. Fig.3.1(b) shows the projected band structure of a photonic crystal with five missing rows of dielectric columns. This wide defect region leads to multimode operation. For the power splitter presented in this paper, the working point is chosen to be at  $a/\lambda_0 = 0.40$ . It is seen that there are four guiding modes at this frequency. The corresponding properties of the four guiding modes are listed in Table 3.1.

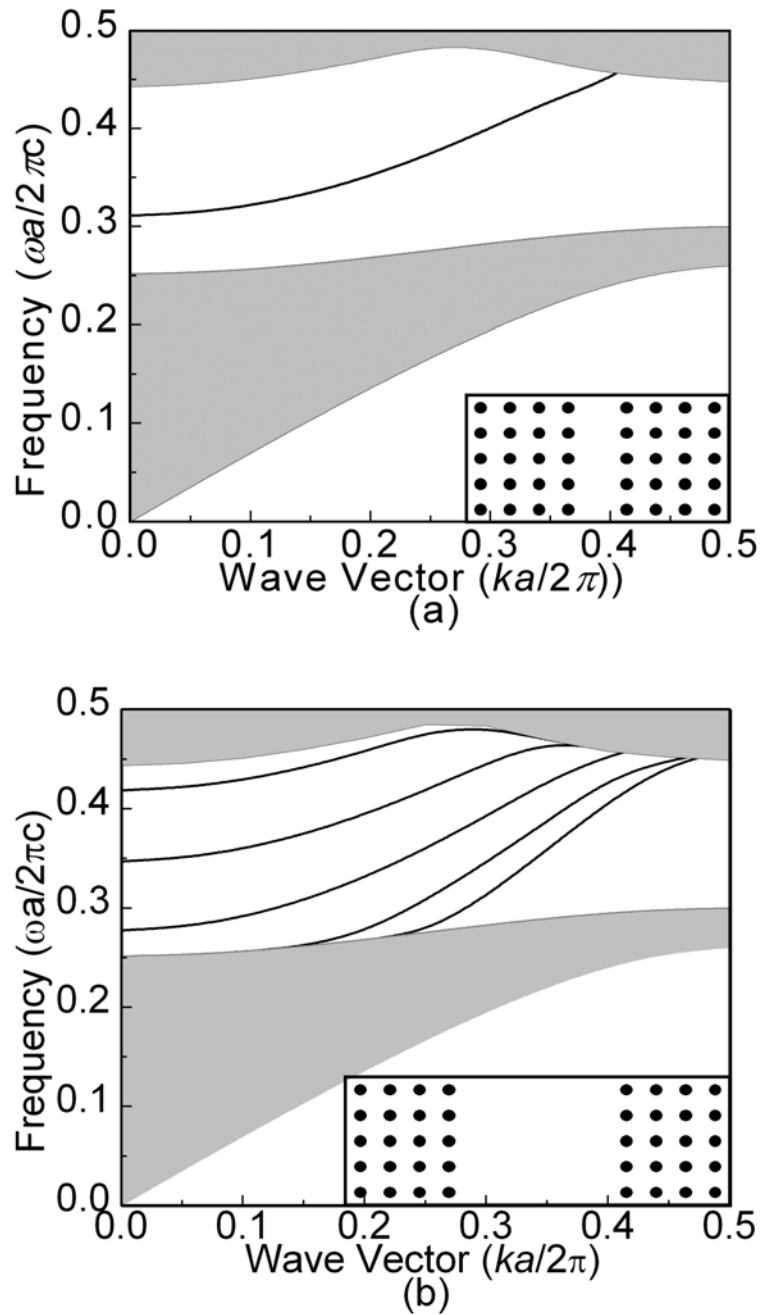


Fig.3.1. Projected band structures of a square lattice of infinite columns ( $\epsilon_{rod} = 11.56$ ) in air ( $\epsilon = 1$ ) with (a) one missing row and (b) five missing rows of dielectric columns.  $r/a = 0.18$  where  $r$ : radius of rods  $a$ : pitch. Both figures are for the TM mode, whose electric field is parallel to the infinite dielectric columns. The insets show the corresponding waveguide structures.

TABLE 3.1

Mode Properties of the Multimode Waveguide in Fig.3.1(b) at the Specified Frequency

Working Point ( $\omega a/2\pi c$ )	0.40			
Mode Number	0 <sup>th</sup>	1 <sup>st</sup>	2 <sup>nd</sup>	3 <sup>rd</sup>
Wave Vector ( $ka/2\pi$ )	0.392	0.363	0.308	0.210
Parity	Even	Odd	Even	Odd

For the  $1 \times 2$  power splitter in this paper, the exciting field entering the multimode waveguide is symmetric. Therefore only two even modes, the fundamental mode and the second-order mode, will be excited. A simple calculation can be done to find the approximate positions of the first single image and two-fold images of the input field. The position of the first single image is approximately  $2\pi/(k_0-k_2) \cong 12a$ , where  $k_0$  and  $k_2$  are the wave vectors for the fundamental mode and the second-order mode respectively. Therefore the position of the first two-fold image is approximately  $6a$ . It should be emphasized here that the length of the multimode waveguide is expected to be only 6 lattice periods to achieve equal power splitting.

In order to assess the performance of such devices, finite-difference time-domain (FDTD) [19] method is used for the simulation. All the FDTD simulations below are for TM light whose electric field is polarized along the axis of the dielectric columns. Light wavelength is chosen to be  $1.55\mu\text{m}$ , a useful wavelength for current telecommunication

systems. Therefore the pitch  $a$  is  $1.55 \times 0.40 = 0.62\mu\text{m}$  and the radius  $r$  is  $0.18 \times a \cong 0.11\mu\text{m}$ .

First we show the MMI effect in photonic crystal waveguides. Fig.3.2(a) shows the symmetric junction connecting a single-mode waveguide with a multimode waveguide. The incident light with the wavelength of  $1.55\mu\text{m}$  is injected from the bottom. The simulation result in Fig.3.2(b) illustrates the MMI effect that is the repetitive appearance of single image and two-fold images of the beam entering the multimode section of the waveguide. The first two-fold image appears about 6 periods away from the junction, and the first single image appears approximately 12 periods away. This simulation result confirms the simple calculation given above.

From the simulation in Fig.3.2, positions of the first two-fold image and therefore the positions of the output waveguides are determined. Fig.3.3(a) shows the ultra-compact waveguide power splitter. This splitter is composed of one input single mode waveguide, one multimode section, and two output single-mode waveguides. The two output waveguides are the same as the input waveguide. They are separated by three rows of dielectric columns and placed at the position of the first two-fold image, which is 6 periods away from the entrance junction. Actually  $6a$  may not be the perfect length for the multimode section. The reason why  $6a$  is chosen for the simulation is that we want to maintain the periodicity for the whole structure. In Fig.3.3(c), it is clear that the input light is equally split into the output waveguides. It should be noted here that the length of

the multimode waveguide is only  $6a$ , which is around  $3.7\mu\text{m}$  in our simulation. The length of  $3.7\mu\text{m}$  is substantially shorter than that of the conventional MMI power splitters, which is usually tens of microns long.

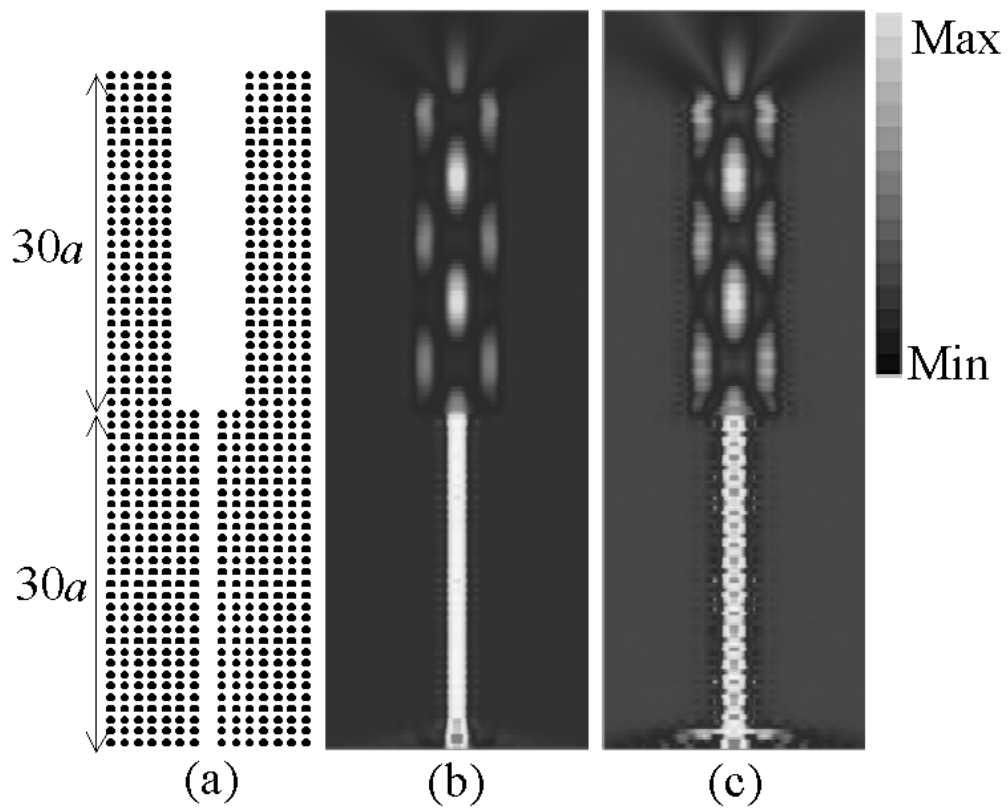


Fig.3.2. (a) Schematic diagram of a junction connecting a single-mode waveguide and a multimode waveguide. (b) Distribution of Poynting vector component along the waveguide direction at  $\lambda_0 = 1.55\mu\text{m}$ . (c) Simulated electric field amplitude distribution at  $\lambda_0 = 1.55\mu\text{m}$ .

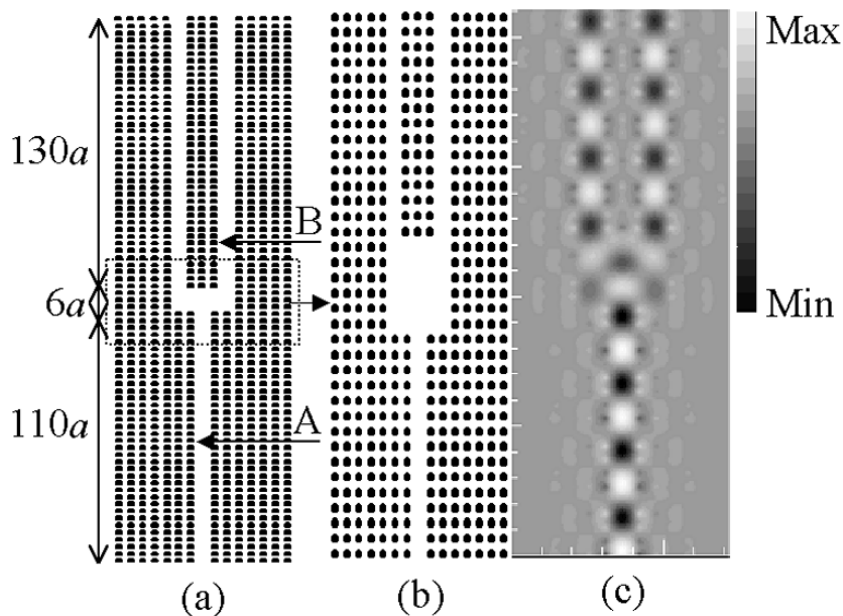


Fig.3.3. (a) Simulated waveguide power splitter. (b) Magnified view of the vicinity of the splitter section. (c) Steady state electric field distribution at  $\lambda_0 = 1.55 \mu\text{m}$  in the vicinity of the splitter section.

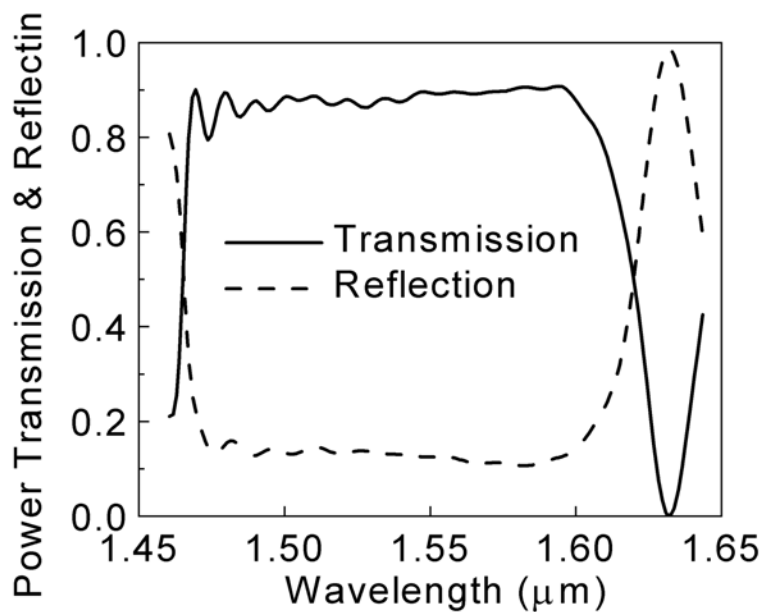


Fig.3.4. Transmission efficiency from the single input waveguide into the two output waveguides and the reflection from the multimode junction.

To calculate the transmission efficiency from the input waveguide into the output waveguides, a large structure with long input and output waveguides is simulated, as shown in Fig.3.3(a). 32 grid points are used to represent each unit length in the FDTD calculation. A pulse centered around  $1.55\mu\text{m}$  is sent into the input guide from the bottom. Field amplitude is monitored at positions A and B. By using a large computational cell and by properly positioning each monitoring point, we can distinguish and separate different pulses propagating in the waveguides. The useful pulses are the input pulse and the pulses reflected by and transmitted through the multimode section. The parasitic pulses are those reflected by the edge of the waveguide. The pulses are then Fourier transformed to obtain the reflection and transmission coefficients for each frequency. Fig.3.4 shows the calculated transmission efficiency from the input into the output waveguides and the reflection by the multimode section. It can be seen that the transmission spectrum is flat in a wide wavelength range and the efficiency is around 0.90, while the reflection is around 0.10. According to our calculation, most of the reflection happens at the junction connecting the input waveguide with the multimode section. This can be explained by the imperfect coupling between the single-mode and multimode waveguides that have only two even modes excited. The remaining reflection happens due to the lateral\_mismatch between the images in the multimode section and the input ports of the output guides and can be minimized by adjusting the positions of dielectric columns close to the input ports of the output guides. This method is applied in the MZI example discussed in the subsequent sections.

The output waveguides of MMI devices are sometimes required to be spaced far enough apart to minimize optical and electrical interaction. For conventional MMI devices based on ridge waveguides, this is usually done by increasing the width of the multimode section. As a result, the beat length and, therefore, the size of the entire device becomes larger. In the photonic crystal-based splitter, this function can be fulfilled by the unique property of photonic crystal waveguide, namely, high transmission efficiency through sharp bends [5], [9].

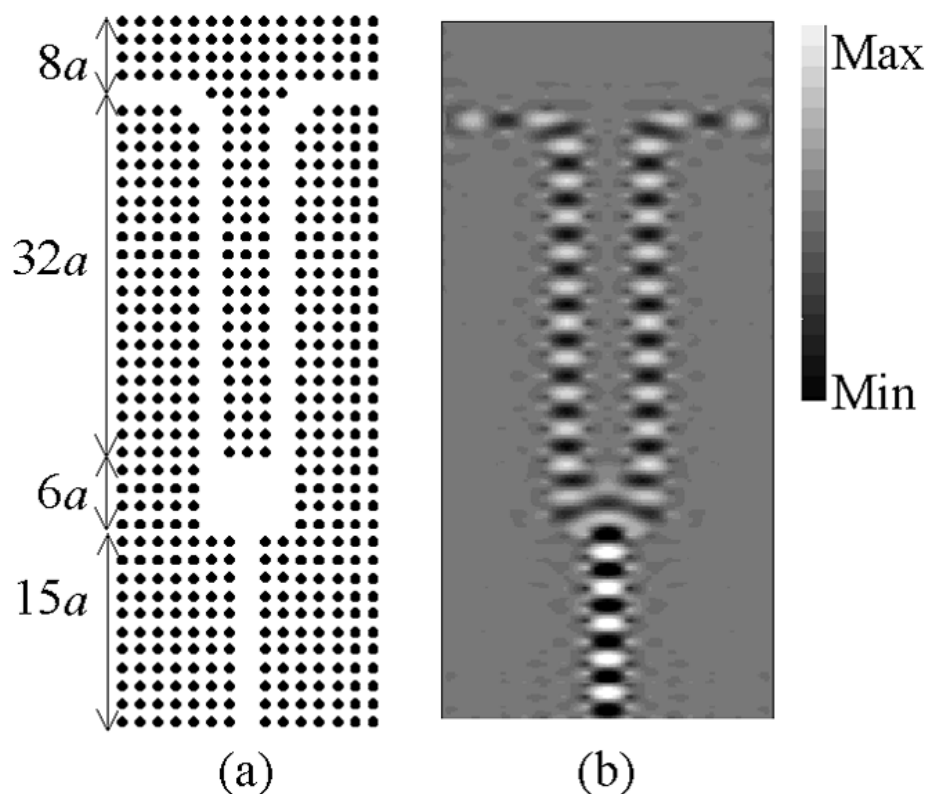


Fig.3.5. (a) Schematic diagram of the compact waveguide power splitter connected with two sharp bends. (b) Simulated electric field distribution at  $\lambda_0 = 1.55\mu\text{m}$ .

Fig.3.5 shows how sharp bends can be used to adjust the separation of the two output waveguides. We use the same method as described in Ref. [5] to calculate the transmission efficiency through the sharp bends and we found that the transmission through the sharp bends in Fig.3.5(a) at  $\lambda_0 = 1.55\mu\text{m}$  is around 0.92. Therefore the transmission efficiency from the input into each output guide after the sharp bends can be estimated to be around 0.42, which is the product of the efficiencies for MMI section and sharp bends.

### **3.3 An Example of Mach-Zehnder Interfometer Based on MMI Power Splitter and Combiner**

Fig.3.6 gives an example of a MZI in a photonic crystal device using MMI power splitter/combiner. In order to improve the efficiency of the MZI, the positions of some columns are adjusted. 3 columns indicated by A and 4 columns indicated by B in Fig.3.6(a) and (b) are moved upward by half a period. In this way, the transmission efficiency of the power splitter is improved by 4% in the vicinity of  $\lambda_0 = 1.55\mu\text{m}$  compared to that without position adjustment according to our calculation. (The efficiency for wavelengths away from  $1.55\mu\text{m}$  is degraded since position optimization cannot be obtained for all the wavelengths simultaneously.)

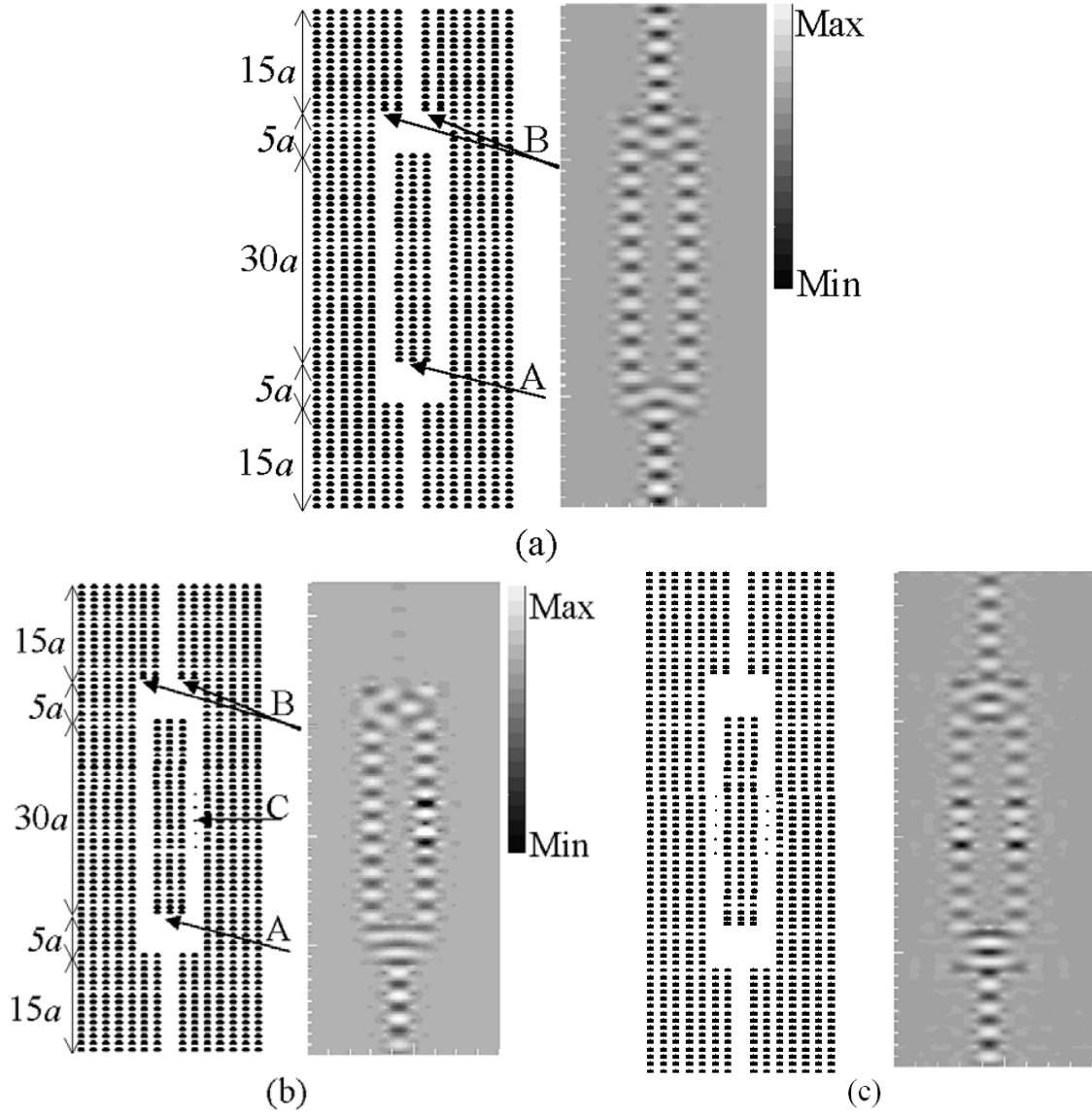


Fig.3.6. (a) Schematic diagram of a Mach-Zehnder interferometer with symmetric arms and the simulated electric field distribution. 3 columns indicated by A and 4 columns indicated by B are moved upward by half period. (b) A Mach-Zehnder interferometer with asymmetric arms and the simulated electric field distribution at  $\lambda_0 = 1.55\mu\text{m}$ . The extra columns indicated by C are located in the central region of the right arm and have the size of  $0.1a$  compared to  $0.18a$  for regular columns. The distance between 2 neighboring extra columns is  $2a$ .  $a$  is the period of the photonic crystal. (c) Mach-Zehnder interferometer with symmetric arms, and the corresponding simulated  $E$ -field distribution. There are five identical extra columns in each arm. Note the high level of transmission. The simulated  $E$ -field distribution is obtained at  $\lambda_0 = 1.55\mu\text{m}$  in all these cases.

In Fig.3.6(a) it is seen that the light is first equally split into the two intermediate single-mode waveguides and then recombined at the output single-mode guide. The transmission efficiency of the structure in Fig.3.6 is calculated using a large structure with very long input guide and output guide in order to avoid the reflections at the two ends. The input and output guides are all  $250a$  long. This large structure is not shown here. Instead, similar structures with short input and output guides and the corresponding field distributions are shown in Fig.3.6 in order to demonstrate the working principle. The ratio of the output to the input is close to 0.90 in Fig.3.6(a), which is comparable to the value given in Fig. 3.4.

In Fig.3.6(b), besides the same column position adjustment indicated by A and B, 5 extra columns with radius  $0.1a$  are inserted into the central region of the right arm of the interferometer. These columns are indicated by C. These extra columns are used to introduce phase shift between the light in the two arms. The light transmission through these extra columns in the right arm at the wavelength of  $1.55\mu\text{m}$  is almost perfect. It can be noticed that light in the two arms is in phase before the extra columns and becomes almost out of phase after the extra columns. Due to the phase shift introduced by the extra columns and the resulting destructive interference, the light in the output guide is barely noticeable.

In Fig. 3.6(c), there are five identical extra columns in each arm. Therefore the

interferometer has symmetric arms and the light coming out of the two arms are added constructively at the output waveguide. High level of transmission is obtained.

The MZI in Fig.3.6 has a limitation of a narrow bandwidth  $\sim 15\text{nm}$  centered around  $\lambda_0 = 1.55\mu\text{m}$ , which is largely imposed by the five extra columns in the right arm. These columns are arranged in such a way that they work like a short coupled resonator optical waveguide (CROW) with a transmission band from  $\lambda_0 \sim 1.40\mu\text{m}$  to  $1.63\mu\text{m}$  lying in the upper region of the band gap. Due to the Fabry-Perot effect of the short CROW-like structure, this transmission window contains multiple peaks, one of which has a width  $\sim 20\text{nm}$  around  $\lambda_0 = 1.55\mu\text{m}$  for good transmission over 90%. Fortunately, the transmission spectrum can be made fairly flat in the window by using the method of adiabatic coupling between a linear photonic crystal waveguide and a CROW [28]. In this way, the bandwidth of the MZI has the potential to be greatly improved.

Even though the design and analysis in this paper were mainly focused on photonic crystals of dielectric columns in air, similar principles may also be applied to their counterparts, i.e. photonic crystals of a low-index material embedded in a high-index background, except for one thing that needs special attention. For MMI devices, the input and output guides are usually designed for single-mode operation, which can be readily achieved in the entire guiding region for crystals of dielectric columns in air by simply removing one row of columns as we have done in this paper. However, in a photonic crystal of air holes in a high-index medium, multiple modes usually exist in the

TE bandgap region after removing one row of air holes. For this case, the structure parameters close to the guide region can be varied to obtain single-mode propagation inside the guiding region [10], [29].

### 3.4 Conclusion

In this paper, we designed and simulated a new compact power splitter/combiner. We have shown that the MMI effect in photonic crystal waveguides can lead to significant device size reduction compared with conventional waveguides. This improvement can be attributed to large dispersion of photonic crystal structures. We also showed an example of the application of the MMI splitter and combiner to a compact Mach-Zehnder interferometer.

## CHAPTER 4

# DESIGN OF A COMPACT PHOTONIC-CRYSTAL-BASED POLARIZING BEAM SPLITTER

### 4.1 Introduction

A polarizing beam splitter (PBS) is an important functional device in optical integrated circuits (OICs). A conventional PBS is usually made in the form of an asymmetric Y-branch [30], a Mach-Zehnder interferometer [31], or a multimode interference (MMI) device [32]. These conventional waveguide PBSs have one common disadvantage: They require relatively long waveguide structures (on the order of millimeters), which imposes limitations on the achievable density of integration.

To reduce the device size, a compact PBS based on a hybrid photonic crystal (PC)/conventional waveguide structure has been proposed [33]. In this design, the light is guided in conventional optical waveguides, while a PC structure acts as a grating to transmit or reflect the light of differing polarizations. Considering the advantages of PC optical circuits, a PBS based on all-PC structures provides the flexibility of easy integration with other PC-based devices and would, therefore, be more attractive. This paper presents the design and numerical analysis of an all-PC based PBS.

There are two requirements to realize a compact, high-efficiency PBS. First, both TM

and TE polarized light must propagate with low loss in the device. Second, the difference between the propagating properties of TM and TE light must be large enough to ensure that the two polarizations can be separated after a short propagation distance. The first requirement might be satisfied by creating the device in a PC with a complete photonic bandgap (PBG) for both polarizations, e.g., a triangular lattice of air holes in a high-index medium with a sufficiently large air-filling factor. However, large air holes are detrimental to waveguiding and lead to losses out of the plane [12]. On the other hand, the size of the PBG, which is defined as the gap-to-midgap ratio, is very narrow for the TM polarization (relative to TE), and that gap could disappear altogether due to fabrication inaccuracies. Furthermore, the difference between TM and TE propagation properties will not be substantial if both polarization states are guided through a similar PBG effect, which would violate the second requirement for a compact PBS.

Fortunately, the PBG effect is not the only mechanism to confine the light in a PC waveguide structure. It has been shown theoretically and experimentally that the light can also be guided through the index contrast in a PC waveguide if the average index in the guiding region is higher than that in the surrounding area [34], [35]. This provides an attractive way for creating a low-loss PC-based waveguide for both polarization states, namely, the PBG effect to confine the TE light, and the index-like effect to confine and guide the TM light. A waveguide of this kind can be realized by removing a row of air holes along the  $\Gamma$ -K direction in a triangular lattice PC that has a PBG for the TE light only. In the defect region (i.e., the missing air holes), the average index is higher than that

in the surrounding region. As a result, while the TE light is being guided through the PBG effect, it might be possible to confine the TM light through the aforementioned index contrast effect. In this way, the first requirement for realizing a compact PBS will be satisfied. Since the TE light and the TM light are now guided by two different mechanisms, we can reasonably expect to find an appreciable difference between the TM and TE propagating properties, so that this difference can be used to separate the two polarization states of the input beam. We use a PC directional coupler to implement the functionality of polarization separation. A PBS based on a conventional directional coupler has been fabricated in the past, with a reported length of 9mm [36]. We show in this paper that polarization separation can be achieved by a PC-based directional coupler over a distance of only 24.2 $\mu$ m.

## 4.2 Design and Analysis

Since most two-dimensional PCs are generally realized in conventional heterostructure slab waveguides, we use the effective refractive index mechanism to confine the light in the third dimension [37] in our finite-difference time-domain (FDTD) simulations [19]. In a high-index-contrast heterostructure, e.g., the SiO<sub>2</sub>/Si/SiO<sub>2</sub> system ( $n_c = 3.6$ ,  $n_s = 1.5$ ), the effective indices for the TM and TE polarizations are very different, which makes it difficult for the TM and TE transmission bands to overlap. However, in a low-index-contrast structure, e.g., a Ga(Al)As laser-like heterostructure, the effective indices for the two polarizations are fairly close to each other. In the latter case, we found it relatively easy to get the TM and TE high-transmission bands to

overlap. We thus consider a two-dimensional PC in a Ga(Al)As laser-like heterostructure corresponding to the carefully studied case of GaAs samples in Ref[38] with the effective refractive index of 3.32 for both polarizations.

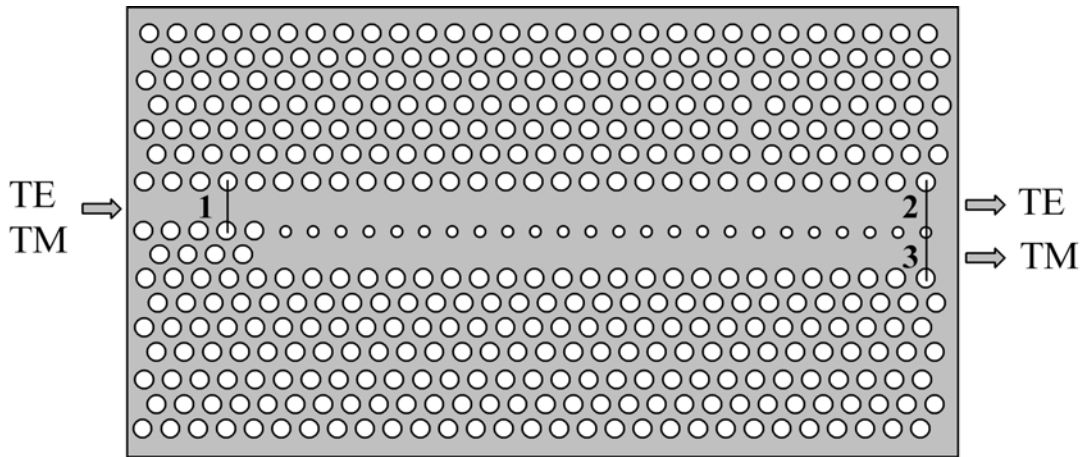


Fig.4.1. Diagram of the proposed PBS based on a PC directional coupler. The effective refractive index of the host material is 3.32; the period of the triangular lattice of air holes is  $a=0.457\mu\text{m}$ ; the radius of the lattice holes is  $r_0=0.147\mu\text{m}$ , while the radius of the smaller holes that separate the two guides in the coupler region is  $r_l=0.118\mu\text{m}$ . The lengths of the input guide and the directional coupler are  $15a$  and  $53a$ , respectively. The top waveguide is referred to as the direct channel, while the bottom guide is called the adjacent channel. Also shown are three line detectors used in the FDTD simulations: 1 to monitor the power input into the directional coupler, 2 to monitor the power in the direct channel, and 3 to monitor the power in the adjacent channel.

The proposed PC-based PBS in a triangular lattice of air holes is shown in Fig.4.1. The single-channel waveguide on the left-hand side (along the  $\Gamma$ -K direction) is used as

the input guide to couple the light into the directional coupler. The coupler consists of two parallel waveguides (i.e., defects in the lattice) separated by a single row of smaller air holes (as compared to the lattice air holes). In this design, the  $E$ -field of the TM light and the  $H$ -field of the TE light are normal to the plane of periodicity. In order to find suitable structural parameters, including the PC period and the radius of the air holes, we began with a large air-filling factor that would give a large TE bandgap. The transmission efficiency was then calculated for both TE and TM light. If we failed to achieve low-loss transmission bands for TM and TE light in such a way that they would overlap over some range of frequencies, the air-filling factor would be reduced until the overlap was found. Further reduction of the air-filling factor would gradually close the TE bandgap, which is not desired for the device performance. The selected period of the triangular lattice is  $a=0.457\mu\text{m}$ ; the radius of the regular air holes is  $r_0=0.147\mu\text{m}$ , and the radius of the small air holes (separating the two guides in the coupler region) is  $r_l=0.118\mu\text{m}$ . By using small air holes to separate the channels, one can improve the coupling strength for TM light, and therefore reduce its beat length and the device size. (In our case, the beat length for TM light is shortened from  $192a$  to  $106a$  when the hole radius is reduced from  $r_0=0.147\mu\text{m}$  to  $r_l=0.118\mu\text{m}$ .) The coupling strength for TE light around the working point does not change much with the reduction of the coupling holes; this point will be discussed later on.

In our FDTD simulations, perfectly matched layers [39] were used to terminate the designed PC structure. A pulse source, centered around  $\lambda=1.55\mu\text{m}$  and having a spatial

gaussian shape, was located at the entrance to the input waveguide; this pulse was used to launch the TM or TE light into the device. In Fig.4.1, three line detectors, one before the directional coupler and marked as 1, another across the direct channel output (marked as 2), and the third across the adjacent channel output (marked as 3), were used to monitor the input and output power levels. The output power was then divided by the input power to compute the transmission efficiency of the PBS at various wavelengths. Note that monitor 1 measures the amount of power that is coupled into the directional coupler; reflection from the directional coupler is thus excluded from the calculation.

Fig. 4.2 shows the computed transmission efficiency of the direct and adjacent channels for TE and TM polarized light. In the FDTD simulations, the length of the coupling region was  $53a$ , where  $a$  is the crystal period. Note that the TM high transmission band ( $>95\%$ ) around  $\lambda=1.55\mu\text{m}$  overlaps with the TE transmission band. It can be seen in Fig.4.2 that for wavelengths in the vicinity of  $\lambda=1.55\mu\text{m}$ , the TE light remains confined to the direct channel, while almost all the TM light is transferred to the adjacent channel. At  $\lambda=1.554\mu\text{m}$ , 98.3% of the TE light remains in the direct channel and 97.6% of the TM light transfers to the adjacent channel. The distributions of Poynting vector along the guide direction for the TE light and TM light are shown in Fig.4.3, where the polarization separation is clearly observed. The operating principle of the PBS is discussed in the next section.

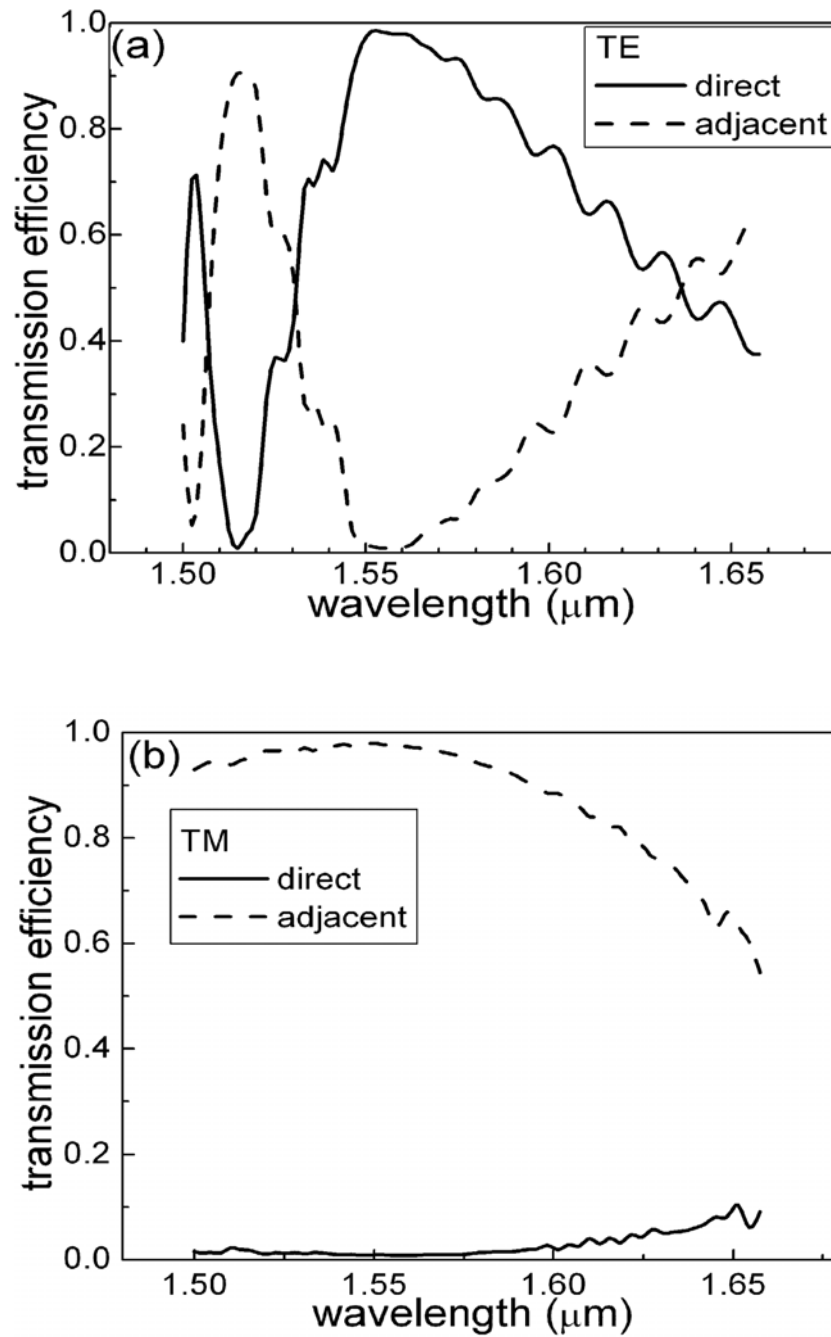


Fig.4.2. Computed transmission efficiency for the direct channel and the adjacent channel for (a) TE light and (b) TM light.



Fig.4.3. Simulated Poynting vector distribution along the guide direction for (a) TE light and (b) TM light in the structure shown in Fig.4.1. The optical wavelength is  $1.554\mu\text{m}$ .

For the directional coupler in the proposed PBS, the two waveguides are decoupled for the TE light [7][40] in the vicinity of  $\lambda=1.55\mu\text{m}$ . This decoupling makes the beat length of the directional coupler extremely large for the TE light. As a result, the TE light remains in the direct channel after propagating through this short device. A careful examination of the Poynting vector distribution of the TE light in the adjacent channel indicates that the field there is not precisely null; see Fig.4.3(a). This is mainly caused by

the slight mismatch between the modal field profiles of the input waveguide and the directional coupler. However, the fact that TE light level remains more or less constant when propagating along the direct channel indicates that the direct and the adjacent channels are actually decoupled. In contrast, the TM light, for which the two channels are tightly coupled, behaves quite differently. This explains why the TM light can transfer completely to the adjacent channel after propagating a distance of half the beat length in the directional coupler (The beat length was found numerically to be around  $106a$ .) The two polarizations are thus separated at the output of the directional coupler into two channels: TE light to direct channel and TM light to the adjacent channel. If necessary, a PC sharp bend may be added at the end of the device to further separate the two polarized beams. Sharp bends with a high transmission efficiency in triangular PCs have been extensively studied [41]-[43] and will not be discussed in this paper.

From Fig.4.2 it can also be seen that the bandwidth for the TE light is much narrower than that of the TM light. This can be explained by the properties of the odd and even modes' dispersion curves for TE light in the vicinity of  $\lambda=1.55\mu\text{m}$  that is close to the upper band edge. From the decoupling point ( $\lambda=1.55\mu\text{m}$ ) to longer wavelengths, the two curves have similar slopes, which causes the slow wavelength routing as shown in Fig.4.2(a). From the decoupling point to shorter wavelengths, however, the slope difference between the two dispersion curves increases dramatically, which explains the rapid wavelength routing in the shorter wavelength regime and hence the small TE bandwidth.

### 4.3 Conclusion

We have presented the design of a compact PBS based on a PC directional coupler in a two-dimensional triangular lattice of air holes in a Ga(Al)As laser-like heterostructure. The polarization separation functionality is enabled by the two different guiding mechanisms: PBG effect for the TE light and index-contrast for the TM light, which makes the two channels of the directional coupler decoupled for TE and tightly coupled for TM light. By utilizing this property, a PBS based on a directional coupler as short as  $24.2\mu\text{m}$  can be realized with the extinction ratios  $\sim 20\text{dB}$  for both TE and TM light.

## CHAPTER 5

# AN INTERSECTION OF NON-IDENTICAL OPTICAL WAVEGUIDES BASED ON PHOTONIC CRYSTALS

### 5.1 Introduction

Photonic crystals have gained worldwide interest, owing to their capability of controlling electromagnetic waves with the existence of photonic bandgap [2]. Various types of optoelectronic devices have been proposed [3]-[4], [20]-[21]. The devices based on photonic crystal structures usually have the advantage of substantial size reduction compared to their conventional counterparts [20], [5]-[7], [22]-[44]. This unique capability may lead to miniaturization and large-scale integration of optical and optoelectronic devices.

Waveguide intersections are useful for constructing integrated optical circuits due to the need for complex lightwave traffic control involving multiple waveguides on a single chip. Johnson et al proposed a scheme to eliminate the cross-talk for a waveguide intersection based on a two-dimensional (2-D) square lattice photonic crystal by using a single defect with doubly degenerate modes [45]. Lan et al suggested a coupled cavity photonic crystal waveguide intersection that utilized the cavity mode profiles to achieve low levels of cross-talk [46]. Based on the method proposed by Johnson et al, Roh et al experimentally demonstrated substantial reduction of cross-talk for a waveguide intersection operating in the microwave regime [47]. Lan et al claimed in Ref [46] that

their design can lead to a 10-nm-wide region with cross talk as low as  $-10$  to  $-45$  dB, while the bandwidth is only  $\sim 7.8$  nm for the method proposed in Ref [45] for comparable cross-talk reduction at the wavelength of  $1.3\mu\text{m}$ . The above designs can give reasonable intersections with large transmission and low cross-talk when the light has a wavelength within the bandwidth ( $\sim 10$  nm). However, if there are two light waves with wavelength spacing greater than about 10 nm that need to cross each other, the above designs will give either low transmission or large cross-talk, which is not desired. In the current optical communication systems, the wavelength band available for use is actually far larger than 10 nm, which creates a need for intersections that can work at much larger wavelength spacings. In this paper we propose a new scheme for constructing such an intersection.

## 5.2 Design and Analysis

The proposed intersection is based on a square lattice of infinitely long dielectric columns in air, as shown in Fig.5.1(a). The columns have dielectric constant  $\epsilon_{rod} = 11.56$  and radius  $r = 0.18a$ , where  $a$  is the column-to-column pitch. With the selected parameters, the 2-D square lattice has a band gap for TM mode in the spectral range  $0.30 \leq a/\lambda_0 \leq 0.44$ ,  $\lambda_0$  being the optical wavelength in free space. By changing the size of a single column surrounded by photonic crystals, one can get an isolated cavity with a certain resonant frequency. Cavities of this kind can be chained together to form a coupled resonator optical waveguide (CROW) [48][49] along  $\Gamma$ -X/X-M directions in the square lattice. Light propagation along the CROW is enabled by photon hopping through the cavities with a transmission band centered at the resonant frequency. Due to the large

interaction between the defect column and the electromagnetic field confined inside the cavity, the defect size can be varied to effectively tune the cavity resonant frequency. Consequently the position of the transmission band moves as well, and it is possible to design CROWs with non-overlapping transmission bands.

In order to determine the transmission band positions, the MIT Photonic-Bands code [18] is used to calculate the projected band structure of the CROW. By carefully choosing the defect size, we obtain two CROWs with non-overlapping bands: one has the defect size of zero (complete removal of the defect columns) with the band from 0.367 to 0.404 ( $2\pi c/a$ ), while the other one has the defect column size of  $0.1a$  with the band from 0.32 to 0.348 ( $2\pi c/a$ ), as shown in Fig.5.1b; here  $c$  is the speed of light in free space. The two CROWs are then arranged to form an intersection as shown in Fig. 5.1(a): the vertical CROW has the defect size of zero, while the horizontal CROW has a defect size of  $0.1a$ . Note that the center of the intersection is a regular column in this case. There is yet another way of forming the intersection with a microcavity, instead of a regular column in Fig.5.1(a), located at the center. This formation, shown in Fig. 5.2, however, will cause serious reflection for either of the two waveguide arms, because the two CROWs have different size of defects and another defect with the size in between the two CROWs must be used in the center position in order to balance the two arms. We have thus concluded that the first method mentioned above is preferred for the intersection design.

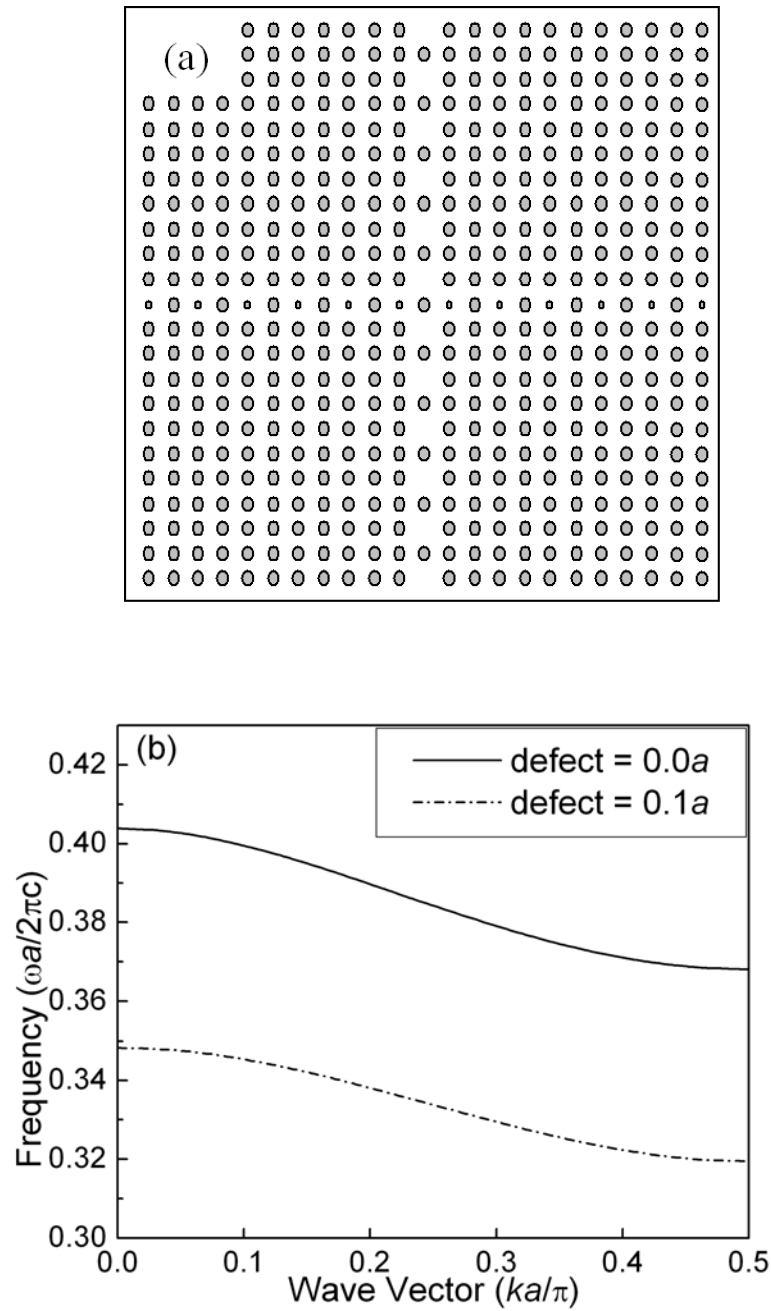


Fig.5.1. (a) Schematic of an intersection based on a square lattice of infinite columns ( $\epsilon_{rod} = 11.56$ ) in air ( $\epsilon = 1$ ).  $r/a = 0.18$  where  $r$  is radius of the columns and  $a$  is the pitch. The defect columns of the vertical CROW are completely removed, while the defect columns of the horizontal CROW have the reduced radius of  $0.1a$ . (b) Projected band structures of the two CROWs for the TM mode, whose electric field is parallel to the dielectric columns.

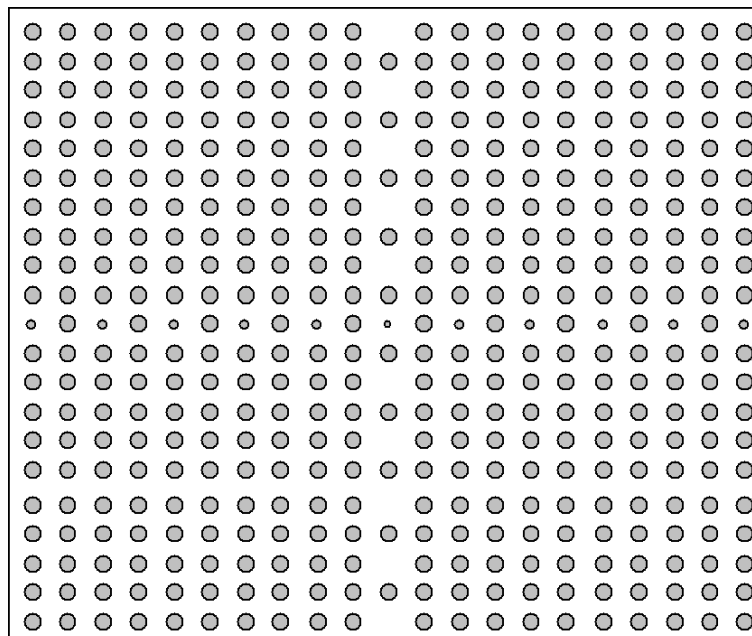


Fig.5.2. Schematic of an alternate intersection with a microcavity at the center based on a square lattice of infinite columns.

Since the two waveguides support non-overlapping transmission bands, light in one waveguide is not allowed to be coupled into the other one, which totally eliminates the cross-talk. Radiation loss is prohibited as well due to the photonic bandgap effect. The only phenomena occurring at the waveguide intersection are thus transmission and reflection. In order to assess the performance of the proposed device, finite-difference time-domain (FDTD) [19] method is used for the simulation. All the FDTD simulations below are for TM light (i.e., electric field along the axis of the dielectric columns). The structural parameters are chosen such that the CROW with the defect size of zero has a

band centered at  $1.31\mu\text{m}$ , while the other CROW has a band centered at  $1.55\mu\text{m}$ . The selected period of the square lattice is  $a=0.512\mu\text{m}$ ; the radius of the regular columns is  $r_0=0.092\mu\text{m}$ ; and the radius of the defect columns (for the horizontal CROW) is  $r_1=0.051\mu\text{m}$ .

To calculate the transmission efficiency of the light through the intersection, two large structures containing an intersection are simulated, as shown in Fig.5.3(a) and (b). In order to save simulation time, the vertical CROW is made shorter when the transmission of the horizontal guide is calculated and vice versa. 120 grid points are used to represent each unit length in the FDTD calculation. Several pulses covering different parts of the transmission band are sent into the input guide from the left. Field amplitudes are monitored at suitable positions before and after the intersection. By using a large computational cell and by properly positioning each monitoring point, we can distinguish and separate different pulses propagating in the waveguides. The useful pulses are the input pulse and the transmitted pulse through the intersection. The parasitic pulses are those reflected at the edge of the waveguide. The pulses are then Fourier transformed to obtain the transmission coefficients for each frequency. The reason why several pulses are used to cover the entire transmission band (instead of a single pulse) is to avoid the rapid spreading out of the single pulse due to large dispersion, which makes it difficult to separate the useful pulses from the parasitic ones.

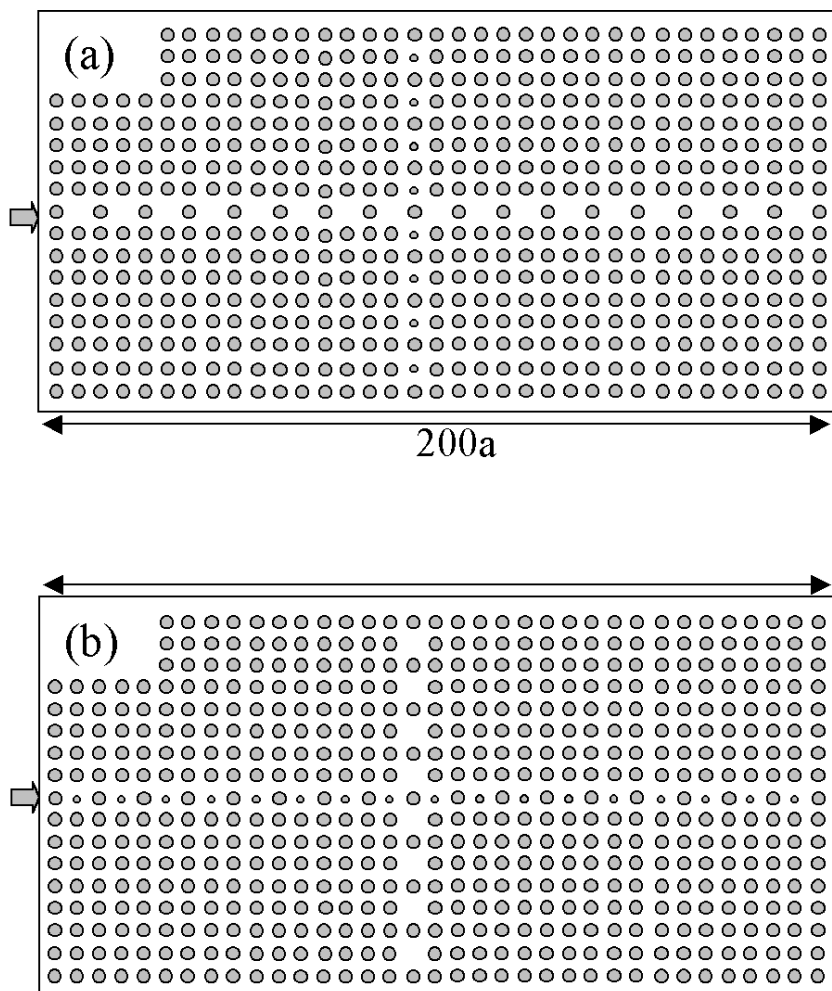


Fig.5.3. Schematic of two structures used in transmission efficiency calculations. (a) is for the vertical CROW and (b) for the horizontal CROW as shown in Fig.1(a). The total length and width of the structures are  $200a$  and  $16a$ , with the intersection  $80a$  away from the left end. One monitor is placed  $41a$  away from the left end, while the other one is  $9a$  to the right of the intersection ( $a$  is the period of the square lattice). Both monitors are located at the center of the cavities.

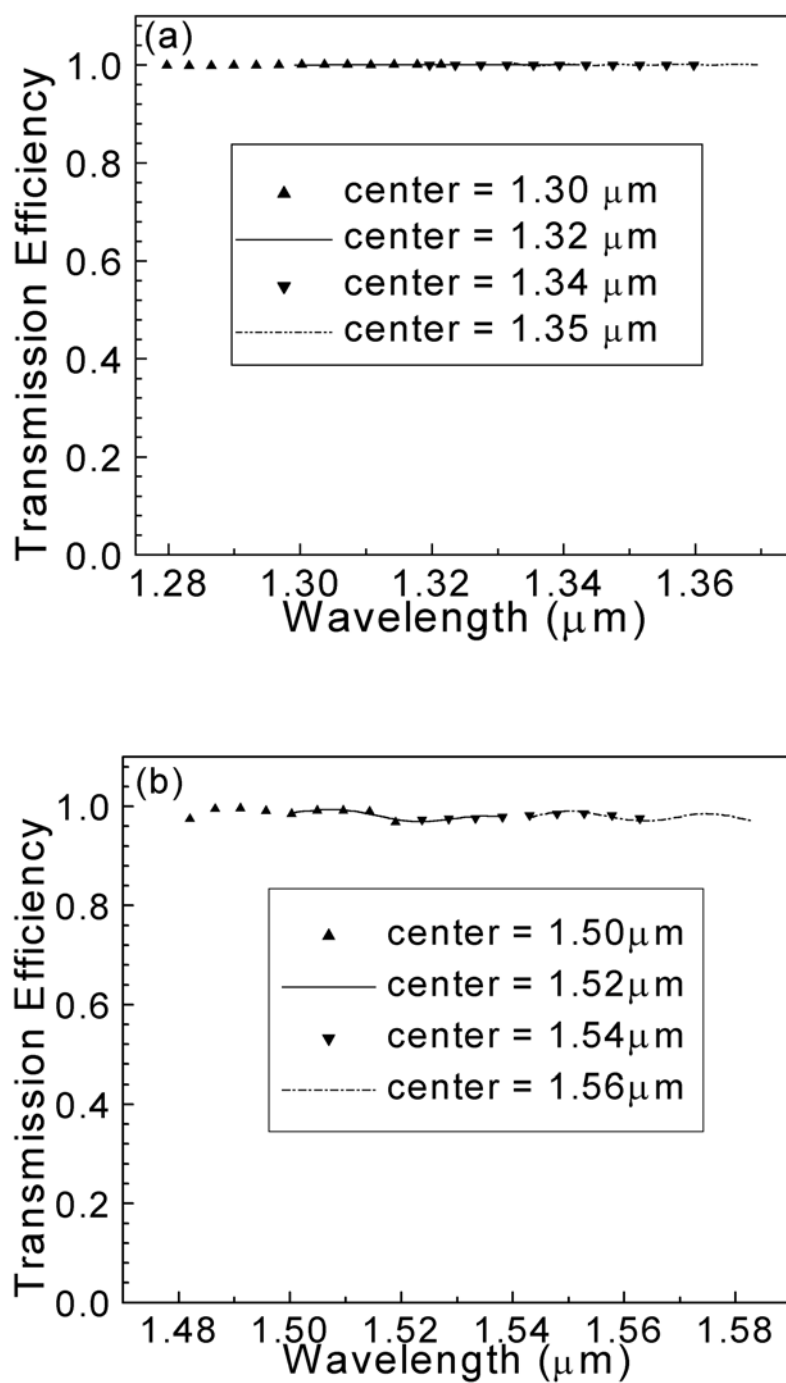


Fig.5.4. Transmission efficiency of the light passing through the intersection for the vertical waveguide (a) and horizontal waveguide (b). Results from different pulses are plotted with different line shapes. Pulse centers are also given.

Figs.5.4(a) and (b) show the calculated transmission efficiencies for the vertical and horizontal arms, respectively. Results from different pulses are plotted with different line shapes. Excellent agreement among neighboring pulses can be seen in the transmission curves. For the vertical waveguide the transmission spectrum is flat and nearly perfect in the entire band from  $1.28\mu\text{m}$  to  $1.37\mu\text{m}$ , while for the horizontal guide the efficiency is slightly below unity ( $>0.96$ ) and exhibits some variation in the band from  $1.48\mu\text{m}$  to  $1.58\mu\text{m}$ . The remaining light in the horizontal waveguide is reflected by the intersection, which can also be observed in the simulations. The fact that the reflection in the horizontal arm is larger than that in the vertical arm can be expected from the design shown in Fig.5.1(a): for the vertical arm, the radius of the two columns closest to the intersection is somewhat reduced (from  $0.18a$  to  $0.1a$ ), while for the horizontal arm, the corresponding columns are totally removed. The sharper structural change in the horizontal arm obviously leads to a larger reflection and, therefore, to lower transmission observed in Fig.5.4(b).

In order to show the performance of the intersection visually, the steady-state field distributions of two light waves propagating along the vertical and horizontal arms in Fig. 5.1(a) are shown respectively in Fig. 5.5(a) and (b). High transmission can be clearly seen.

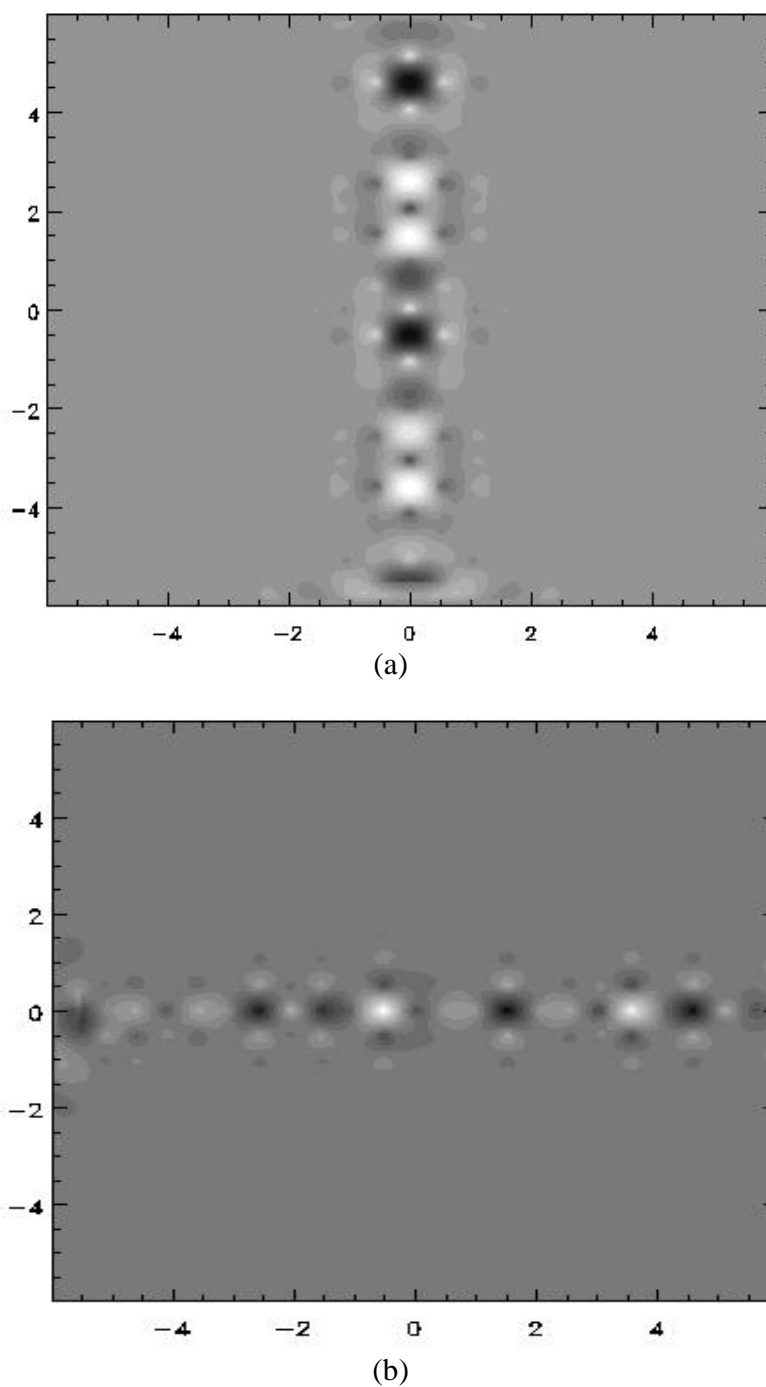


Fig.5.5. Simulated  $E$ -field distribution of (a) vertical arm at  $1.31\mu\text{m}$ , and (b) horizontal arm at  $1.55\mu\text{m}$  corresponding to the structure in Fig. 5.1(a). For the vertical propagation, light is incident from the bottom; for the horizontal propagation, light is incident from the left.

Even though the design and analysis presented in this paper were mainly focused on photonic crystals of dielectric columns in air, similar principles may also be applied to their counterparts, i.e. photonic crystals of a low-index material embedded in a high-index background. In that case, the size of the holes adjacent to or in the middle of the cavity, instead of the column size used in this paper, can be varied to tune the transmission band's position, which also makes it possible to create CROWs with non-overlapping bands. Detailed discussions of this type of CROWs can be found elsewhere [50] and will not be discussed in this paper.

### **5.3 Conclusion**

We proposed a new waveguide intersection for light waves with a large wavelength spacing based on photonic crystal CROWs with non-overlapping transmission bands. Light within the two bands can propagate through the intersection with nearly perfect transmission and with low cross talk. This design is for the purpose of accommodating the wide transmission band in the current optical communication systems.

# CHAPTER 6

## DESIGN OF PHOTONIC CRYSTAL COUPLED- RESONATOR-OPTICAL-WAVEGUIDES WITH SINGLE MODE PROPAGATION IN THE BANDGAP

### 6.1 Introduction

Photonic crystals have gained worldwide attention in the past few years. They have the ability to control electromagnetic waves due to the existence of photonic bandgap [1][2]. The coupled resonator optical waveguide (CROW) has recently received much attention due to its special properties: narrow band transmission and slow group velocity [48][49][51]. This slow wave property may play an important role in enhancing nonlinearities and wave interactions.

In many practical applications, single mode operation is desirable. For a CROW based on photonic crystal structures of dielectric pillars in air, it is easy to get single mode operation because the waveguide width is much smaller than the light wavelength [49][52]. But one drawback of these types of CROW structures is that light cannot be confined in the third dimension because the guiding region is air, which cannot provide index guiding. Therefore in this paper we choose photonic crystals of air holes in a

dielectric material to study such devices. For a CROW defined in such photonic crystals, light can be confined in all three dimensions.

In Ref[50], the authors give a method to design a single mode CROW along the  $\Gamma$ -M direction in a triangular lattice photonic crystal. For that case, a complete row of air columns along  $\Gamma$ -M direction is removed. Actually for studies of line defect linear waveguides in triangular lattice photonic crystals,  $\Gamma$ -K direction waveguides receive much more attention than those along  $\Gamma$ -M direction [53][54][55]. Therefore it will be beneficial for the integration of conventional line defect linear waveguides and CROWs in triangular lattice photonic crystals if we can design single mode  $\Gamma$ -K direction CROWs.

In this paper, we propose another way to achieve the goal.

## 6.2 Design and Analysis

The refractive index of the host material for our triangular lattice is chosen to be 3.4, which is for silicon in the infrared regime. Radius of the air holes,  $r$ , is chosen to be  $0.32a$ , where  $a$  is the period of the triangular lattice. The MIT Photonic-Bands code [18] is used to calculate the dispersion diagrams of the photonic crystal structures. With the selected parameters, the 2-D triangular lattice has a band gap for TE mode in the spectral range  $0.216 \leq a/\lambda_0 \leq 0.298$ ,  $\lambda_0$  being the optical wavelength in free space. The magnetic fields for TE modes are normal to the plane of periodicity. Fig. 6.1(a) illustrates of a CROW defined in the above triangular lattice photonic crystal of air holes. Every other

air hole is removed along the  $\Gamma$ -K direction. Fig. 6.1(b) shows the unit cell that is used to calculate the dispersion diagram and mode profiles of the CROW. There are two transmission bands in the photonic band gap (PBG) region, which can be clearly seen in the dispersion diagram of Fig. 6.1(c). These two transmission bands are crossed and cover different frequency ranges. The reason for the existence of two crossing bands is that there exist two degenerate modes, even and odd, for an isolated cavity. If we bring two identical cavities close to each other, even modes of the two neighboring cavities will have a larger overlap than the odd modes. Consequently even modes have stronger coupling than odd modes and therefore the even transmission band covers a wider frequency range.

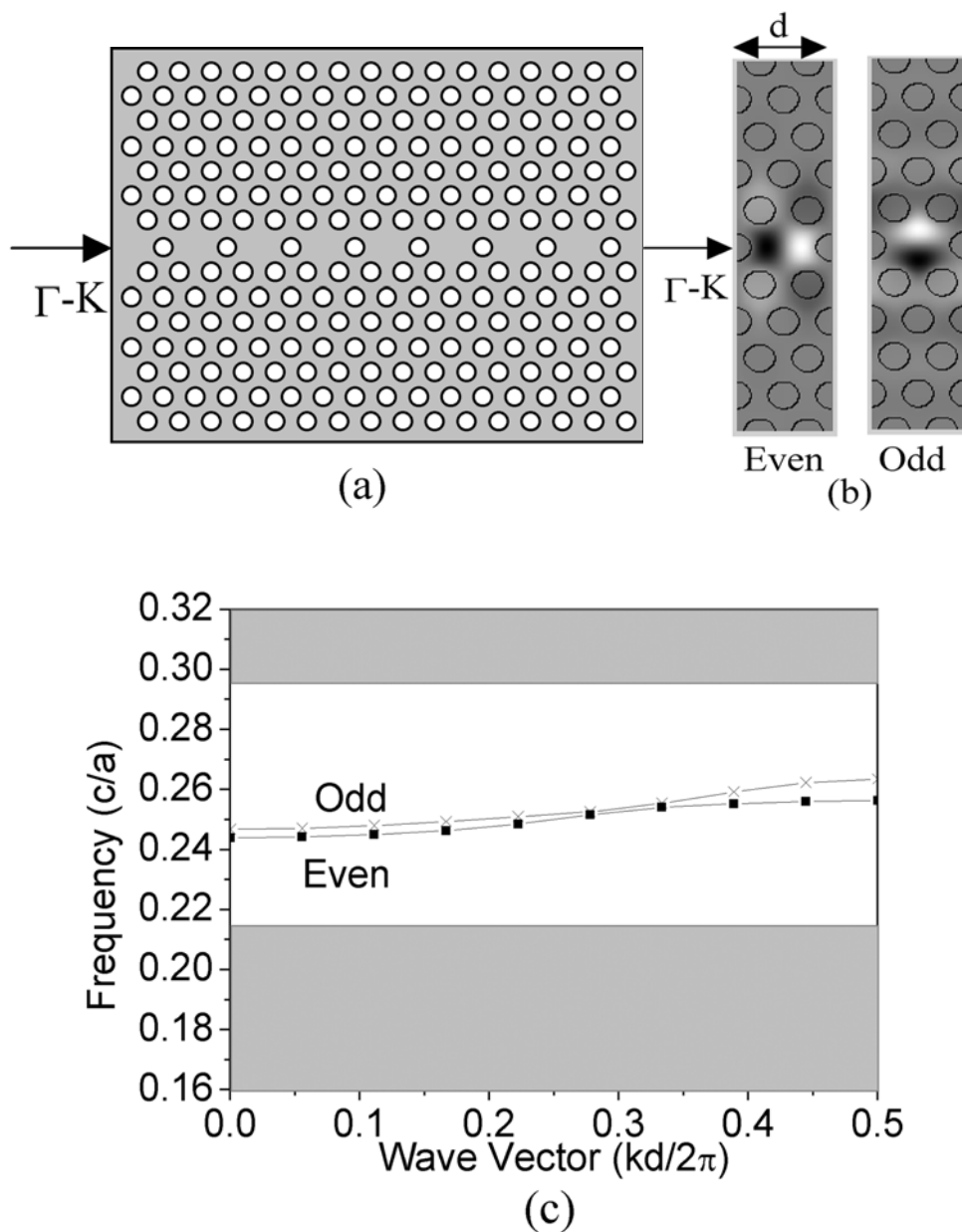


Fig. 6.1. (a) A CROW along the  $\Gamma$ -K direction of a two-dimensional triangular lattice photonic crystal of air holes in silicon with refractive index of 3.4. (b) One unit cell and the mode profiles of the even and odd TE modes of the CROW. (c) Dispersion diagram of the CROW in the photonic bandgap.  $r/a = 0.32$  where  $r$ : radius of air holes  $a$ : pitch. The magnetic fields for both TE modes are normal to the plane of periodicity.  $d$  is the pitch of the CROW. In this case,  $d = 2a$ .

From the above analysis it can be seen that pure size change of neighboring holes cannot achieve a satisfactory single even mode transmission band in the PBG region for  $\Gamma$ -K direction CROW made in triangular lattice photonic crystal. Let us then have a close look at the mode profiles in Fig. 6.1(a). It is obvious that both even and odd modes have a node centered in the cavity. The node of the even mode is perpendicular to the waveguide direction, while the node of the odd mode is along the waveguide direction. Therefore insertion of an anisotropic air hole in the center of the cavity may have different effects on the two modes. We try the anisotropic defect hole shown in Fig. 6.2(a). This hole is composed of two semi-circles at both ends and a rectangle in the middle. This shape is compatible with practical fabrication. Since the purpose is to get single even mode transmission band in the PBG region, the odd mode band has to be pushed out of the PBG region totally. For this reason, the direction of the anisotropic defect hole should be arranged such that it will have a larger effect on the odd mode. Comparing the two mode profiles in Fig. 6.1(a), we can see that the direction of the anisotropic defect hole should be perpendicular to the waveguide direction. With this arrangement, the defect hole has a much larger overlap with the odd mode than with the even mode and therefore affects the odd mode more.

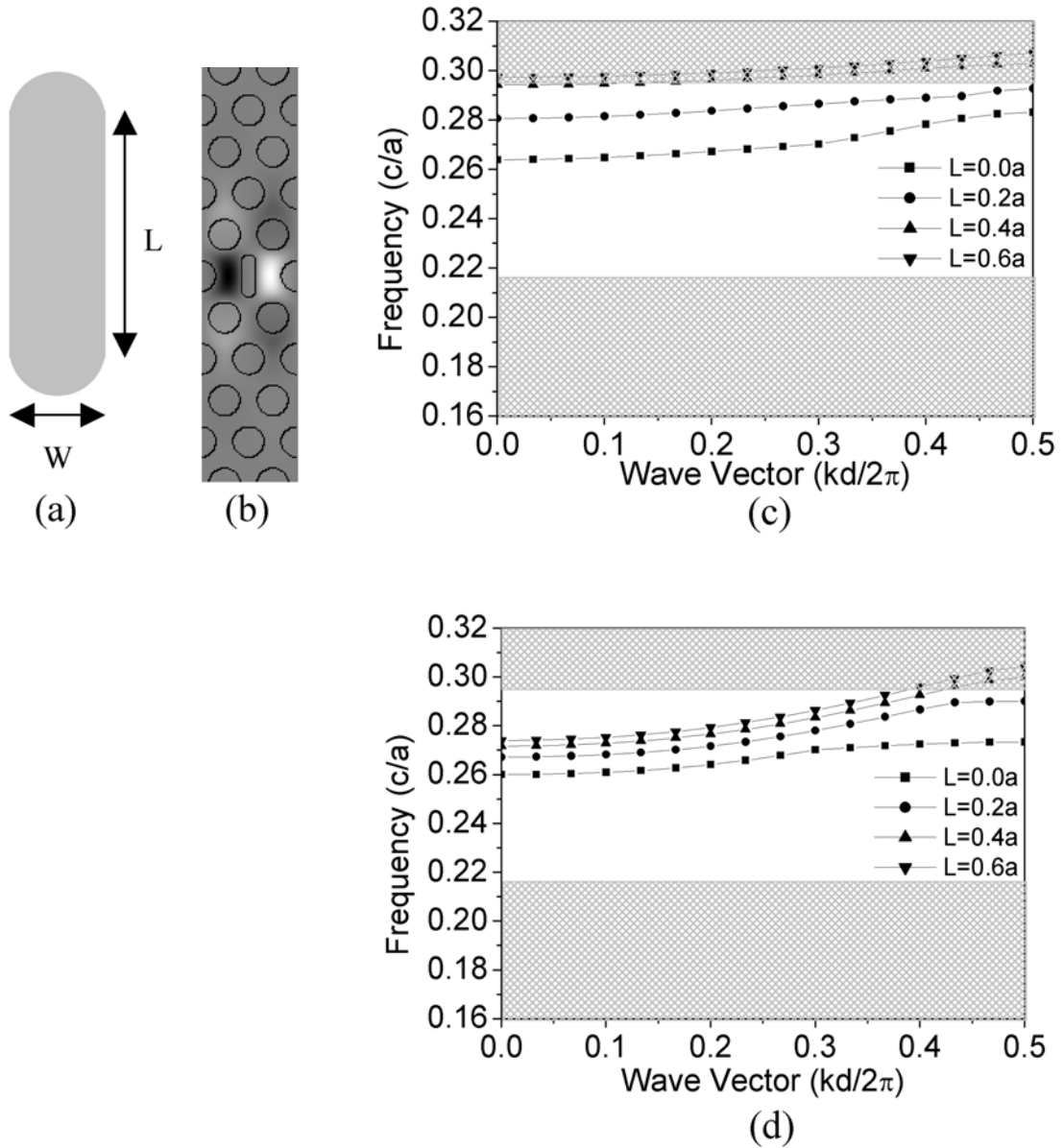


Fig.6.2. (a) Shape of the anisotropic defect hole.  $W$  is the width of the rectangle and the diameter of the two semi-circles.  $L$  is the length of the middle rectangle. (b) The even mode profile for the modified CROW with  $w = 0.3a$  and  $L = 0.6a$ . All the other holes have the radius of  $0.32a$ . (c) The odd TE mode for several sizes of the defect. (d) The even TE mode for several sizes of the defect. The magnetic fields for both TE modes are normal to the plane of periodicity.  $d$  is the pitch of the CROW. In this case,  $d = 2a$ .

The width  $W$  of the defect hole and also the diameter of the two semi-circles are chosen to be  $0.3a$  such that the modification has little effect on the even mode. The length  $L$  of the defect hole is increased gradually from 0 to  $0.6a$  so we can see how the even and odd modes evolve. Evolution of the odd TE mode is shown in Fig. 6.2(c). The odd band is pushed upward when the defect hole length is increased and disappears completely from the PBG region finally. As shown in Fig. 6.2(d), the even mode is also pushed upward, but it moves much more slowly than the odd mode. For the case of  $L = 0.6a$ , we get only a single even mode in the whole PBG region, as desired.

### 6.3 Conclusion

We presented a way to design a single mode  $\Gamma$ -K direction CROW in a triangular lattice photonic crystal of air holes in a dielectric. It is shown that insertion of an extra anisotropic hole along a specific direction in the cavity can lead to single even mode transmission in the whole PBG region, which is important for many practical applications.

# CHAPTER 7

## FABRICATING TWO-DIMENSIONAL PHOTONIC CRYSTALS WITH EMBEDDED DEFECTS USING BLUE-LASER-WRITER AND OPTICAL HOLOGRAPHY

### 7.1 Introduction

Photonic crystals (PCs)[1][2], which attracted significant attention in recent years for their unique characteristics, hold the promise for the construction and integration of optical components in a very compact manner. In order to realize functional PC devices like optical waveguides [13] and microcavities [14], various defect structures have to be incorporated into the otherwise periodic structures. However, due to the extreme difficulty to make the necessary defects in three-dimensional (3D) PCs, most researchers have been focusing on two-dimensional (2D) PCs on slab platforms [13]-[15].

Currently, electron beam lithography is a commonly used technique for fabricating 2D PCs with high degree of accuracy and design flexibility [13]-[16]. However, direct-write E-beam lithography is a slow and expensive process, which makes it inappropriate for the mass production of large integrated optical circuits. By comparison, optical holography is an ideal candidate for making PCs with high throughput on a large area.

But optical holography itself can only produce PCs without any defect structures that are necessary for realizing functional optical components. Taking advantage of the negative photoresist nature of SU-8, L. Pang et al. used a strongly focused UV laser beam to introduce linear defects into PCs produced by optical holography [56]. Since in this method the selective exposure by the focused UV laser beam happens after the holography and before the resist development, it is difficult to differentiate the unexposed area from those exposed and thus difficult to find the right location for the defects. The other problem is that the selective exposure not only defines the defects, but also changes the size of the holes adjacent to the defect region, which is not desired.

In this paper, we describe a new method to produce PCs with controlled defects by combining a custom-built blue-laser-writer (BLW) and the technique of optical holography. In our method, the defect patterns are defined onto the substrates through direct laser writing and lift-off process before the optical holography. Therefore, the defects are actually visible during the following holography process, which is potentially useful for the alignment between the defects and the PCs. It is also shown that this process has very little effect on the size of the holes adjacent to the defect regions. Finally we propose an interferometry-based method for the strict alignment between the pre-defined defects and the PCs.

## 7.2 Blue-Laser-Writer Optical System

The blue laser writer (BLW) optical system can be used for maskless microfabrication. A substrate is first coated with photoresist, and then the desired patterns are defined into the photoresist through direct laser writing. After development, wet or dry etching is used to transfer the patterns from the photoresist into the underlying substrate. A picture of the entire system is shown in Fig. 7.1.

The entire system is mainly composed of three parts: interferometers for stage movement control, auto-focus part for maintaining the sample at focus, and the writing part for suitable exposure. The sample is placed on a stage that is moved with high-resolution picomotors and monitored by two interferometers. The blue laser beam with the wavelength of 400nm is focused on the sample through an objective lens.

The interferometers part is shown in Fig. 7.2. A HeNe laser is used here. Because the output power of HeNe laser is not very stable, a reference detector shown as Det. 1 in the Fig. 7.2, is used for the monitoring purpose. There are two interferometers: one for X-axis, the other for Y-axis. The interferometer signals are acquired by the computer and fitted to obtain the moving distance of the stages.

Fig. 7.3 shows the auto-focus and the writing parts. Signals from the quadruple detectors are acquired by the computer and it is determined if the sample is in focus or not. If the sample is still in focus, writing will continue; if the sample is out of focus, the

picomotor of Z direction will move the stage up/down to find the focal position and then the writing will continue.

Fig. 7.4 shows the schematic of the control system for the blue-laser-writer optical system. Picomotors for X, Y, and Z directions are connected to the parallel port through a network controller; Detectors 1, 2, and 3 for the interferometers, and quadruple detector for the auto-focus part are connected to a data acquisition (DAQ) board and then to the computer; the blue laser for the writing is connected to the computer through a serial part.

By controlling the blue laser output power, the exposure time at each point, and the numerical aperture (NA) of the lens, different linewidth can be obtained. Fig. 7.5 shows such an example. In this example, a pre-cleaned glass slide was coated with positive photoresist Shipley1805. The final thickness of the photoresist is around  $0.5\mu\text{m}$ . Several straight lines were written into the photoresist by the blue laser writer optical system. The output power from the blue laser is  $1.0\text{mW}$ , and the actual power on the sample for the writing is  $50\text{nW}$ . NA of the objective lens used here was 0.6. The length of each line is  $50\mu\text{m}$ . The writing was done point-by-point and the point spacing was  $1\mu\text{m}$ . The exposure time at each point was increased from 10ms to 500ms. It can be seen that the linewidth increases with the exposure time.



Fig. 7.1 Picture of the entire blue-laser-writer optical system.

## *Interferometers*

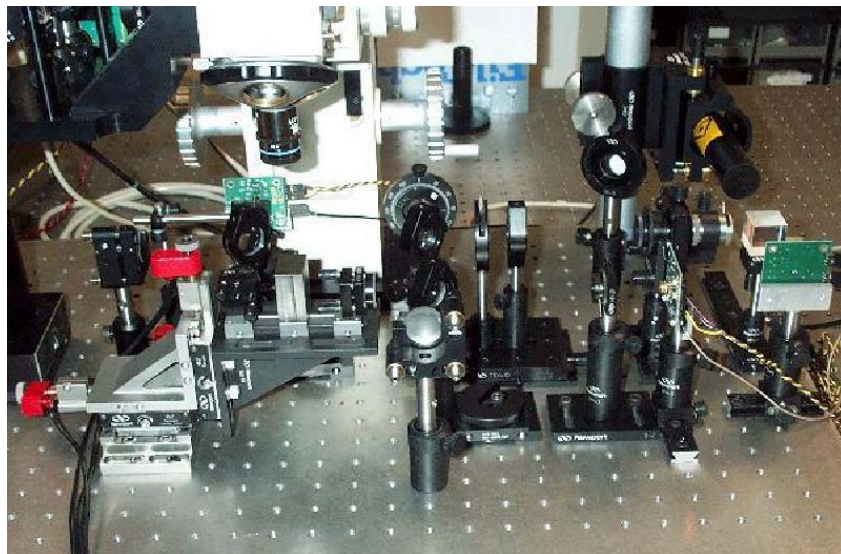
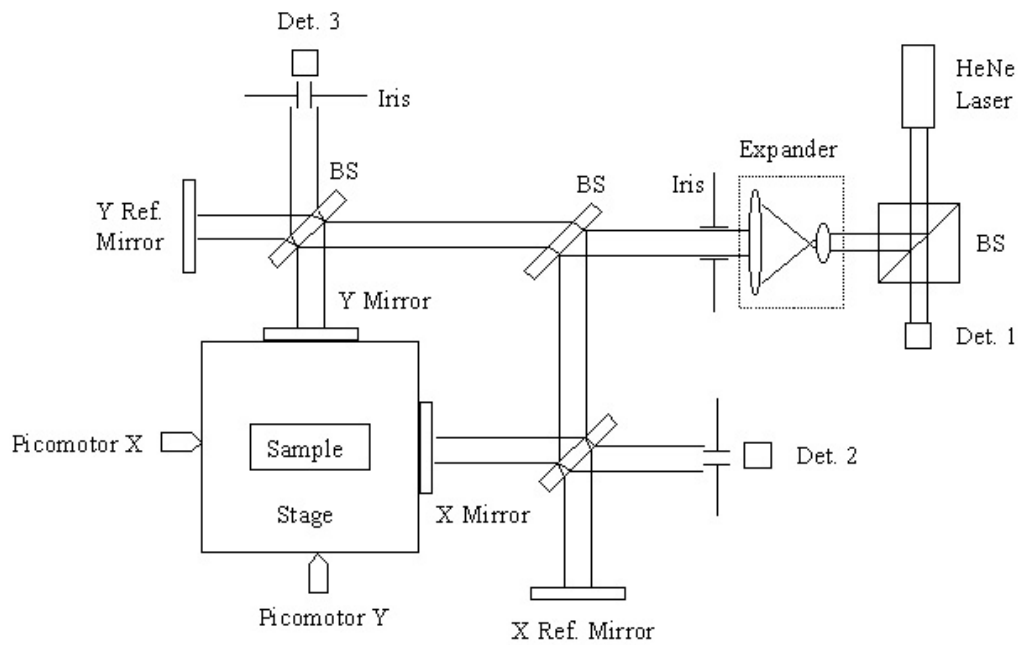


Fig. 7.2 Schematic and a picture of the interferometers setup. A HeNe laser is used here. There are two interferometers: one for X-axis, the other for Y-axis.

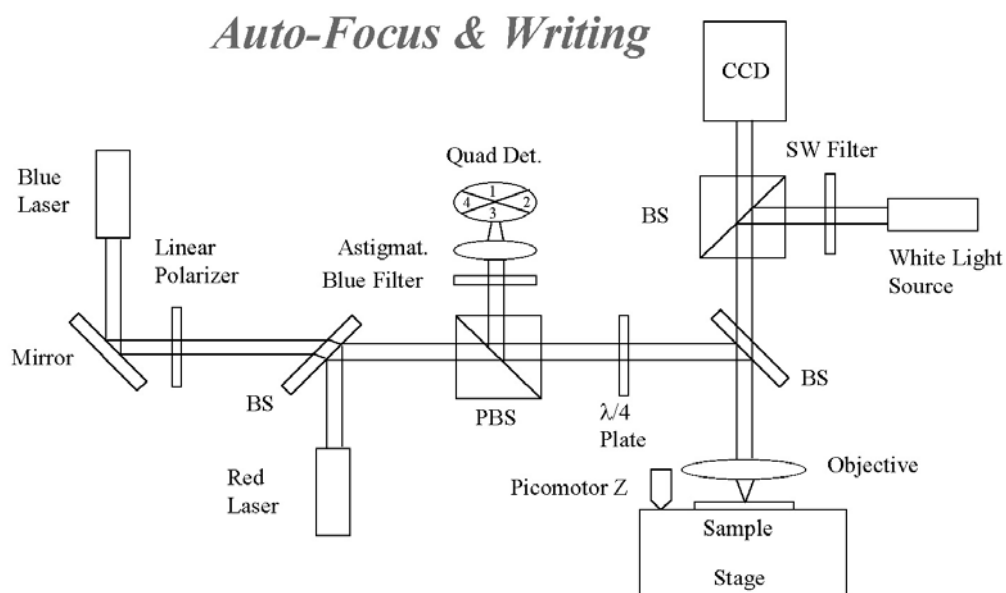


Fig. 7.3 Schematic and a picture of the auto-focus and writing setup. A blue laser is used for writing and a red laser is used for auto-focus.

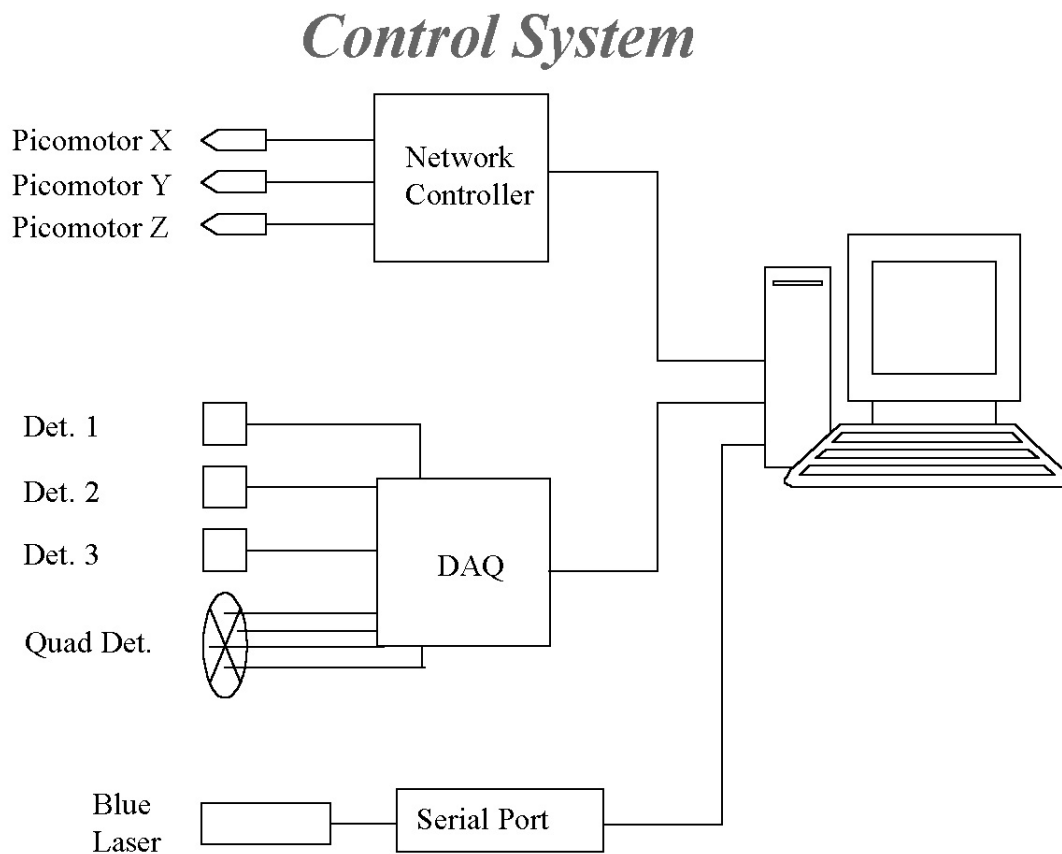


Fig. 7.4 Schematic of the control system for the blue-laser-writer optical system. Picomotors for X, Y, and Z directions are connected to the parallel port through a network controller; Detectors 1, 2, and 3 for the interferometers, and quadruple detector for the auto-focus part are connected to a data acquisition (DAQ) board and then to the computer; the blue laser for the writing is connected to the computer through a serial port.

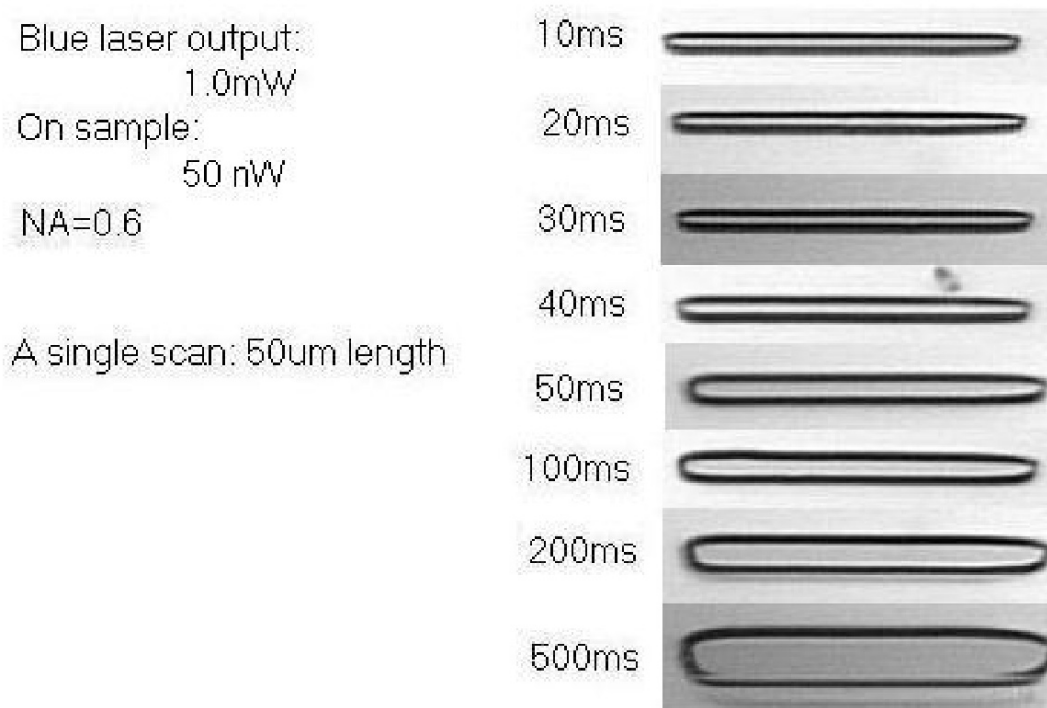


Fig. 7.5 Pictures of several straight lines written into photoresist by the blue laser writer optical system. Pictures were taken after development in 351. The output power from the blue laser is 1.0mW, and the actual power on the sample for the writing is 50nW. The numerical aperture (NA) used here is 0.6. The length of each line is 50 $\mu$ m. The writing is done point-by-point and the point spacing is 1 $\mu$ m. With the exposure time at each point increasing from 10ms to 500ms, the linewidth increases as well.

### 7.3 Optical Holography System

The optical holography (two-beam interference) setup is schematically shown in Fig.7.6. He-Cd laser has two emitted wavelengths: 325nm and 441.6nm. In our experiment, 441.6nm is used because the optics in our setup is transparent at 441.6nm. The laser beam is routed by two metallic mirrors, expanded by a spatial filter, and then collimated. Top half of the beam is reflected by a mirror and then reaches the sample, while the bottom half of the beam illuminates the sample directly. The two beams combine on the sample and create the interference pattern. The mirror and the sample holder are mounted at  $90^\circ$  on the same rotational stage. By adjusting the orientation of the stage, we can easily change the incident angle of the laser beam onto the sample and thus the period of the interference patterns. The period is determined by this formula:  $\lambda/[2\sin(\theta/2)]$ , where  $\lambda$  and  $\theta$  are the laser wavelength and the angle between the two beams incident on the sample. A square lattice PC pattern can be created by exposing the sample twice with a rotation of  $90^\circ$  before the second one.

Two examples of photonic crystal patterns fabricated by the optical holography are shown in Fig. 7.7. The period of the square lattice is  $1.0\mu\text{m}$ . An InP substrate was first coated with positive photoresist Shipley1805. The final thickness of the photoresist was around  $0.5\mu\text{m}$ . After being exposed by the optical holography, the sample was developed in 352 developer. From Fig. 7.7, it can be seen that perfect circular holes can be created and the hole size can be adjusted by changing the exposure time.

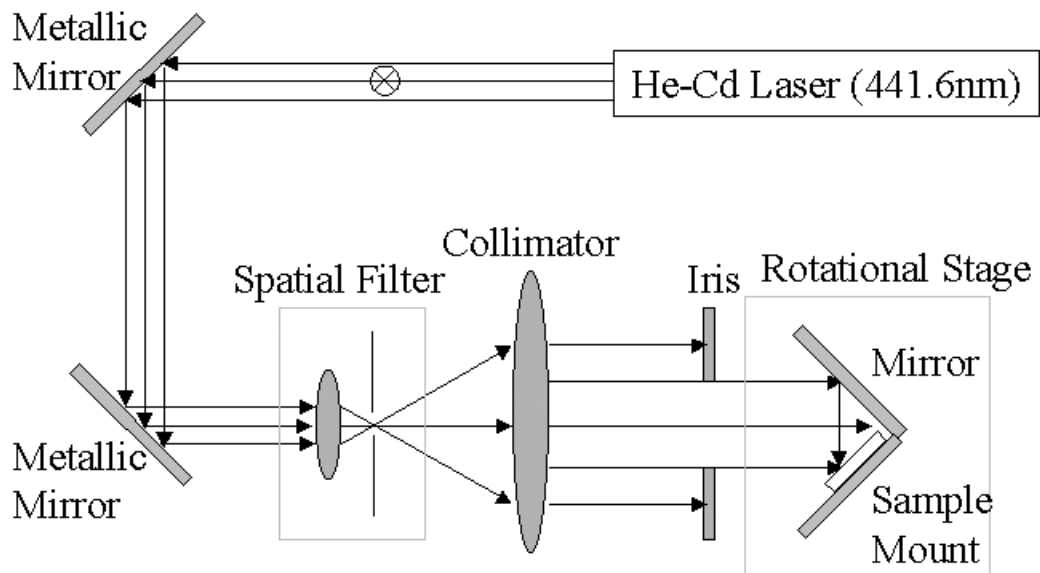
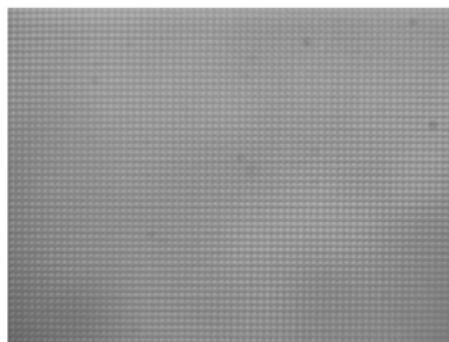


Fig.7.6 Schematic of the two-beam interferometric optical holography. The laser emits two wavelengths: 325nm and 441.6nm. Two filters in front of the laser can be used to select the desired wavelength. 441.6nm is used in our experiment because the optics is not transparent at 325nm. The direction of polarization of the laser beam is normal to the plane. Objective lens in the spatial filter: X60/0.85; Pinhole in the spatial filter:  $5\mu\text{m}$ ; Collimator: F5/250mm. The iris after the collimator selects the central uniform part of the collimated beam. Another metallic mirror and the sample holder are mounted on the same rotational stage with 90 degrees.

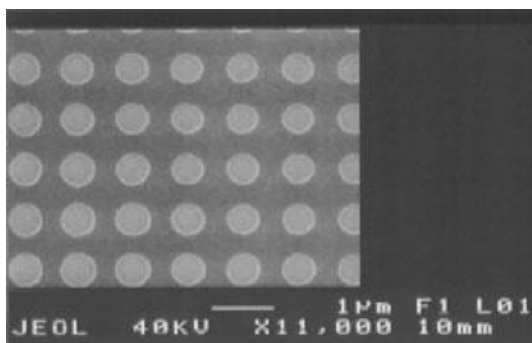
## *2D Photonic Crystals Fabricated by Holography*



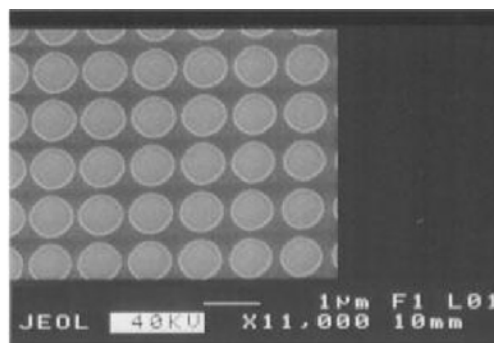
Period  $\sim 1.5\mu\text{m}$



(a)



**Small exposure**



**Large exposure**

(b)

Fig. 7.7 Pictures of photonic crystals fabricated by optical holography: (a) pictures taken under an optical microscope for overall view; (b) Scanning Electron Microscope (SEM) micrographs for two different exposures. The period of the square lattice is  $1.0\mu\text{m}$ . The photonic crystal patterns are in the photoresist after development.

#### 7.4 Fabricating Two-Dimensional Photonic Crystals with Defects

The primary steps of our method are schematically shown in Fig. 7.8. The substrate is (100)-InP. First, the InP substrate is coated with a thin Chromium (Cr) layer deposited by E-beam evaporator and a layer of positive photoresist (Shipley1805) by a spin coater. The thicknesses of the Cr layer and the photoresist are 40nm and 500nm, respectively. Then the defect patterns are defined into photoresist through direct blue laser writing. After the resist development, a SiO<sub>2</sub> layer 60nm thick is deposited on the photoresist by E-beam evaporator and patterned by lift-off process. The above process is illustrated from Fig.7.8(1) to (4). In the figure, only a linear defect is shown for the purpose of demonstration. Various defects can be defined through the above process. Now the defect regions on the substrate are protected by the SiO<sub>2</sub> layer and the sample is ready for the subsequent optical holography.

Another layer of photoresist is spin coated onto the sample with the pre-defined defects. 2D PCs are then created on the above sample through optical holography with dual exposures. After resist development, the PC pattern is then transferred into the Cr layer by wet etching while the Cr layer under the pre-defined SiO<sub>2</sub> defect regions is protected. After the wet etching, the residual photoresist is removed by O<sub>2</sub> plasma. SEM micrographs of the PC with defects in Cr are shown in Fig. 7.9. The SiO<sub>2</sub> area is clearly visible in the figures. The next CH<sub>4</sub>-H<sub>2</sub>-based ECR-RIE dry etching process transfers the PC patterns from Cr to the underlying InP substrate. The protective SiO<sub>2</sub> layer also etches

during the dry etching process. Finally, the residual Cr is chemically removed. The above process is illustrated from Fig.7.8(5) to Fig.7.8(8).

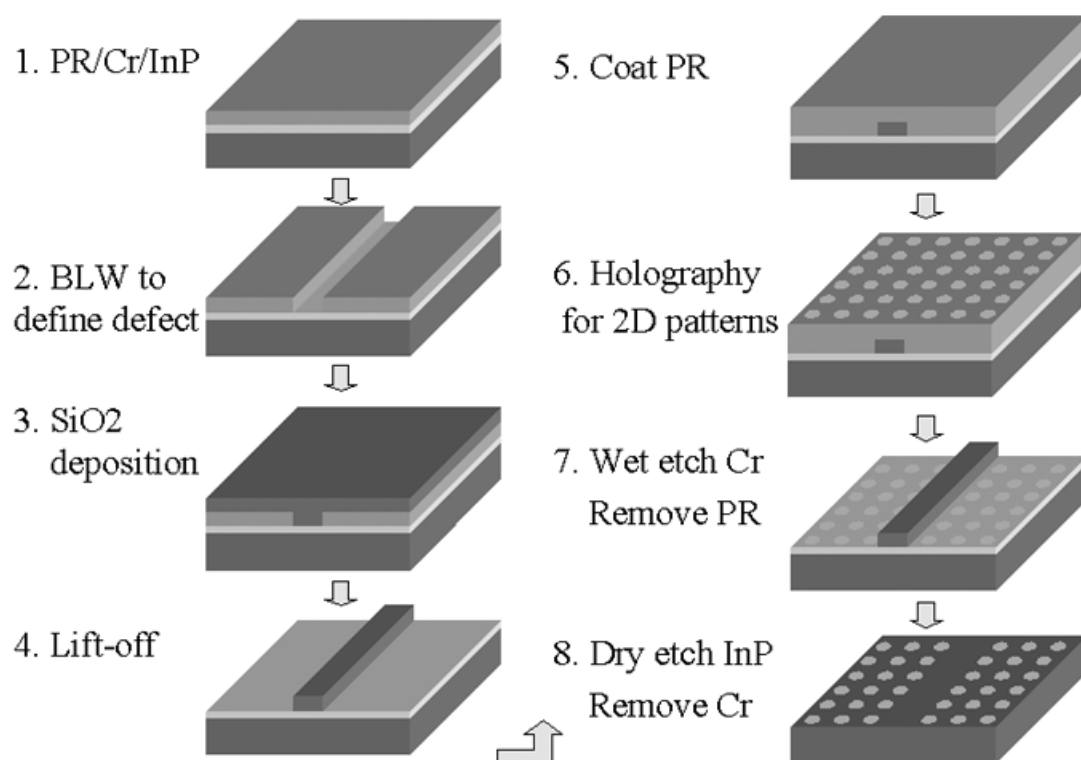


Fig.7.8 Schematic of the fabrication procedures for creating defects into photonic crystals. PR: photoresist; BLW: blue laser writer.

In our experiment, two defect structures, a linear defect and a Y-junction, are used for the purpose of demonstration. Because the linewidth of the defects that can be obtained with the BLW is around  $1\mu\text{m}$ , the period of the PC is chosen to be  $1\mu\text{m}$  in order to demonstrate a linear defect with only one row of holes missing. The SEM micrographs of the final PC patterns with defects in InP are shown in Fig. 7.10. The cross sectional views of the final PC patterns with two different dry etching time are shown in Fig.7.11: (a) 30 min, and (b) 60 min. The etch depths are about  $0.5\mu\text{m}$  and  $1.0\mu\text{m}$ , respectively. It can be seen from Fig. 7.10 that the size of the holes adjacent to the defect region is almost the same as those away from the defects. This fact shows that our process has little effect on the size of the holes close to the defect regions.

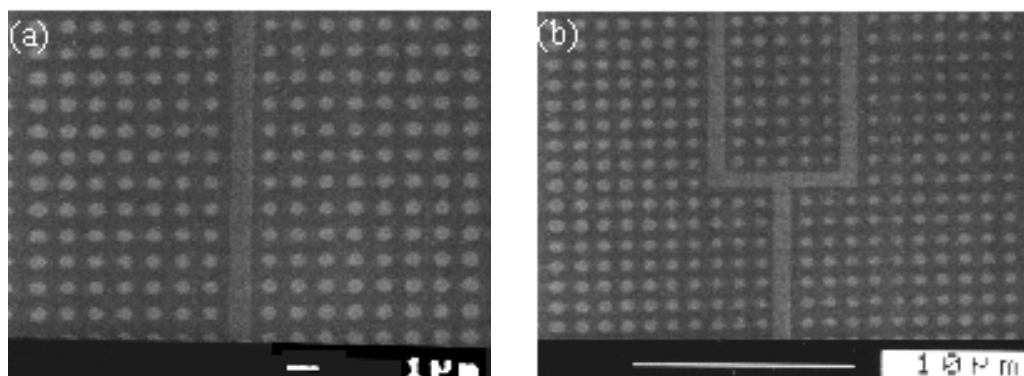


Fig. 7.9 SEM micrographs of the PCs with defects in Cr. These figures are corresponding to Fig.7.8(7). The SiO<sub>2</sub> layer in the defect regions is clearly visible.

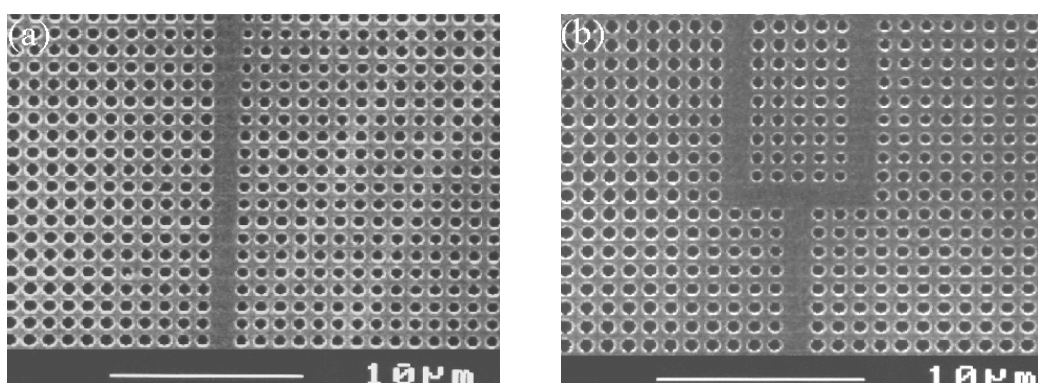


Fig. 7.10 SEM micrographs of the PCs with defects in InP. These figures are corresponding to Fig.7.8(8).

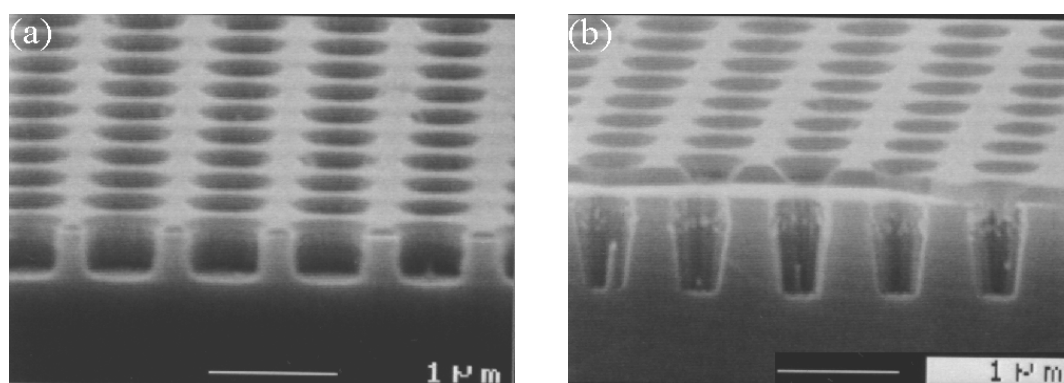


Fig. 7.11 Cross sectional view of the PCs in InP after dry etching for (a) 30 min; (b) 60 min. These figures are corresponding to Fig.7.8(8).

## 7.5 Measurement

In the last section, we demonstrated the fabrication of photonic crystals with controlled defects by combining the blue laser writer and optical holography. The chosen period of the photonic crystal was  $1.0\mu\text{m}$  in order to demonstrate a single linear defect. (This linewidth is determined by the resolution of the blue laser writer.)

In order for the device to work at the wavelength around  $\lambda=1550\text{nm}$  for the current optical communication system, the period of the photonic crystals has to be reduced to  $\sim 500\text{nm}$ . In this section, a beam splitter based on a square lattice photonic crystal with the period of  $500\text{nm}$  was fabricated and measured. But due to the resolution limitation of the blue laser writer, a single linear defect waveguide could not be made. Instead, seven rows of air holes were missing intentionally. The fabrication procedure is the same as last section.

The employed substrate is shown in Fig.7.12. Light confinement in the vertical dimension is ensured by a  $420\text{ nm}$ -thick GaInAsP layer with a photoluminescence peak at  $1.22\ \mu\text{m}$ , capped by an InP protective layer (thickness =  $200\text{ nm}$ ). The effective index is around 3.21.

The schematic of the measurement setup is shown in Fig. 7.13. The light source is Agilent tunable laser with the tuning range from  $\lambda=1460\text{nm}$  to  $\lambda=1580\text{nm}$ . A fiber polarization controller is used to control the polarization of the light incident on the

sample. A lensed fiber is used to couple the light into the photonic crystal structure. An objective lens is used to collect the light from the output of the tested structure and to image the output facet onto an IR camera. In order to measure the output power, another lensed fiber will be used instead to collect the output light and send it to a power meter.

In Fig.7.14, pictures of the fabricated photonic crystal beam splitter and the measurement result are shown simultaneously. In this beam splitter, seven rows of air holes were missing, which is corresponding a defect width  $\sim 3.5\mu\text{m}$ . In order to couple the light in and out of the device, the sample was cleaved from both sides. Prior to cleaving, the sample was thinned from  $350\mu\text{m}$  to  $180\mu\text{m}$ . This thinning process enables us to obtain smooth cleaved edges at both sides of the device, which helps improve the coupling in and out of the device. The total length of the device after the cleaving is  $\sim 200\mu\text{m}$ . The separation between the two output waveguides is  $100\mu\text{m}$  such that the output signals from the output waveguides can be easily distinguished from the light that is not coupled into the waveguide.

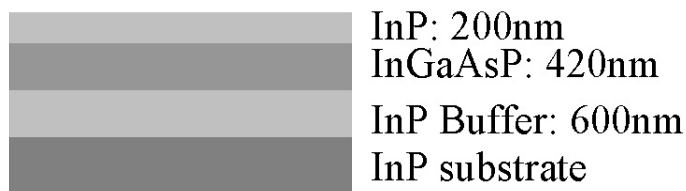


Fig. 7.12 Schematic of the InP-based heterostructure for the fabrication of the photonic crystals with defects for the measurement.

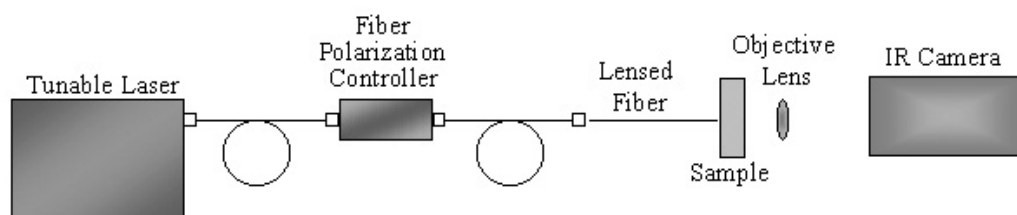


Fig. 7.13 Measurement setup for the fabricated photonic crystal device.

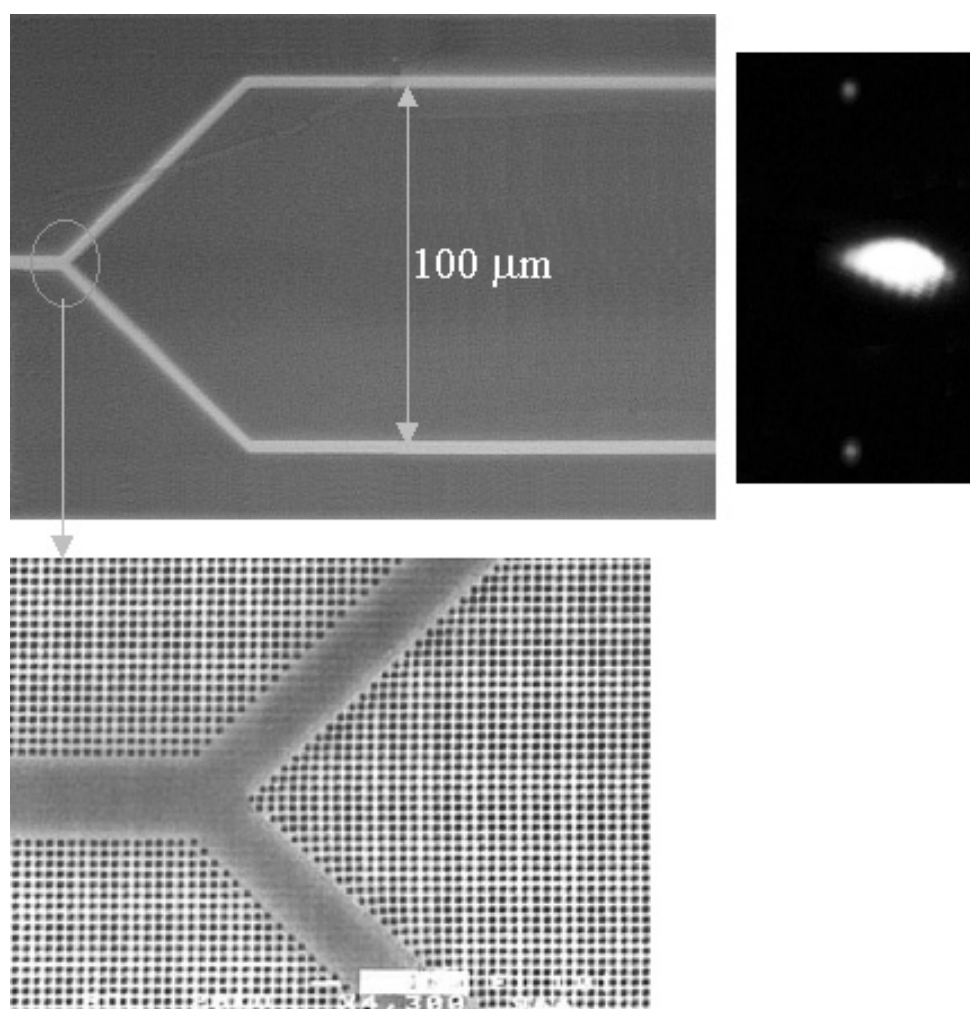


Fig. 7.14 Beam splitting at  $\lambda=1540\text{nm}$  for TE polarization. Top: picture of the fabricated beam splitter (taken with an optical microscope); Bottom: SEM micrograph of the splitter region; Right: signals detected by an IR camera placed at the output end of the splitter for in-plane view.

In the right picture of Fig.7.14, the signals coming out of the two output waveguides can be clearly seen and are separated from the light that is not coupled into the waveguide. The output power from a single output waveguide is measured to be around  $2\mu\text{W}$  with the help of another lensed fiber. The low output power compared to the incident light ( $4\text{mW}$ ) is explained below.

For the square lattice fabricated into the InP-based low-index contrast waveguide structure, there is just a very small and incomplete bandgap for TE polarized light at the wavelength of  $1550\text{nm}$  (no bandgap for TM polarized light). Due to the low index contrast between the cladding and the guiding layer, almost all the guiding modes of the waveguide structure are above the light lines of the cladding, which results in radiation loss during the light propagation in the device [57]. This explains why the output power from the output waveguides is very low compared to the incident power. This problem can be solved by two possible ways. First, a high index contrast waveguide structure [13] should be used instead of the low index contrast InP heterostructure. This way, most of the guiding modes could be below the light line and the radiation loss could be suppressed. Second, triangular lattice photonic crystal should be fabricated instead of the square lattice. Linear defect waveguides fabricated into InP low-index contrast can give truly guiding modes below the light line. This way the radiation loss could be suppressed as well.

## 7.6 Discussion and Conclusion

Even though the results shown in this paper give an excellent alignment between the defects and the PCs, these results are difficult to repeat due to the alignment problem. As described above in the process, the defects are first defined and therefore, they are visible during the subsequent holography process, which makes the strict alignment between the defects and the PCs possible. We propose a way for this purpose. In this way, two lasers will be used during the holography process: 325nm light from He-Cd laser and 650nm from a HeNe laser. Obviously, the period of the interference pattern produced by the 650nm light is twice that of the 325nm light for the same incident angle. The two laser beams can be aligned so that the two sets of patterns overlap. Since the positive photoresist (Shipley1805 in our experiment) is insensitive to light at 650nm, this light can be used for aligning the defects and PCs with the help of monitoring equipments like CCD camera. After the alignment is finished, light at 325nm can be turned on to expose the photoresist. The fact that the light at 650nm gives the interference pattern with a larger period makes the alignment easier than that with the light at 325nm.

In this paper, we developed a new method to fabricate PCs with embedded defects by combining a custom-built blue laser writer and the technique of optical holography. For the purpose of demonstration, two defect structures, a linear defect and a Y-junction, surrounded by square lattice PCs are defined into InP substrate. If desired, a triangular lattice can also be fabricated with  $60^\circ$  sample rotation in between. It is also shown that this method has little effect on the size of the holes adjacent to the defect regions, which

is a desirable feature. Finally, taking advantage of the fact that the defects are visible during the holography process, we proposed a way for the strict alignment between the defects and the PCs, We believe that, with this method, various defects can be fabricated to produce different functional PCs at low cost and large volume.

## CHAPTER 8

# TRANSMISSION MEASUREMENT ON PHOTONIC CRYSTAL WAVEGUIDES FABRICATED ON InP BASED SUBSTRATES

Photonic crystals (PCs) are capable of controlling light at the scale of optical wavelength and make large-scale integrated optical circuits possible. Two-dimensional (2D) PCs fabricated in InP substrates allow the implementation of photonic integrated circuits that could then include active devices. One important issue for the application of PCs is how to couple the light from external sources to PCs with high efficiency. In our preliminary experiments we adopted a more or less common approach: a conventional ridge waveguide was used to route the light into and out of the PC. Compared to silicon-on-insulator (SOI) substrates, the InP substrate has a larger vertical modal dimension, which facilitates the in- and out-coupling.

Light confinement in the vertical dimension is ensured by a 420 nm-thick GaInAsP layer with a photoluminescence peak at 1.22  $\mu\text{m}$ , capped by an InP protective layer (thickness = 200 nm). Our 2D PCs consist of a triangular array of air holes with period  $a = 0.45 \mu\text{m}$ , which results in a bandgap around  $\lambda = 1.5 \mu\text{m}$ . Our PC patterns are defined with e-beam lithography in PMMA, then transferred into a  $\text{SiO}_2$  layer that is used as a mask for  $\text{CH}_4$ -based ECR-RIE etching. The fabrication procedures are shown in Fig. 8.1.

The PC linear defect waveguide (Fig. 8.2a) is constructed by removing a single row of holes along the  $\Gamma$ -K direction. The top view of the PC interface is shown in Figs. 8.2(b) and 8.2(c), with the SEM cross-sectional views of the ridge and the PC appearing in Figs. 8.2(d) and 8.2(e). The samples are subsequently lapped and cleaved for the final measurement.

Ridge waveguides, gradually tapered from a width of 4  $\mu\text{m}$  at the sample facet to 1  $\mu\text{m}$  at the PC interface, are used to couple the light in and out of the PC waveguide with the help of two tapered lensed fibers; see Fig. 8.3(a). To eliminate the direct coupling between the input and output lensed fibers, an S-bend structure (Fig. 8.3) is adopted such that the displacement between the two lensed fibers is  $\sim 400 \mu\text{m}$ . This reduces the optical direct coupling between the two fibers to below the noise level. A tunable laser (Agilent 8164A) with a range of  $\lambda = 1460 - 1580 \text{ nm}$  is used as the light source, and an optical spectrum analyzer (ANDO AQ6315E) is used to measure the transmitted light. A polarizer with an extinction ratio  $\sim 38 \text{ dB}$  and a fiber polarization controller are combined to control the polarization of the incident light.

Two adjacent waveguide structures having the same length were fabricated on the same substrate: one is just a ridge waveguide without an embedded PC structure for calibration purposes (see Fig. 8.3b), while the other is a ridge waveguide with a PC device somewhere along the path (Fig. 8.3c). The transmission spectrum of the structure that contains the PC device was normalized to that of the ridge waveguide without the PC. In this way, the input/output coupling loss (from the ridge waveguide to the PC

waveguide and vice versa) as well as the loss within the PC device itself could be evaluated. A preliminary measurement result of the insertion loss versus  $\lambda$  for the TE-polarized light is shown in Fig. 8.4. The minimum insertion loss of  $\sim -5$  dB is seen to occur around  $\lambda = 1540$ nm. Further experiments are in progress to improve the fabrication process and the quality of the devices, so that the measurement results can be compared with computer simulations.

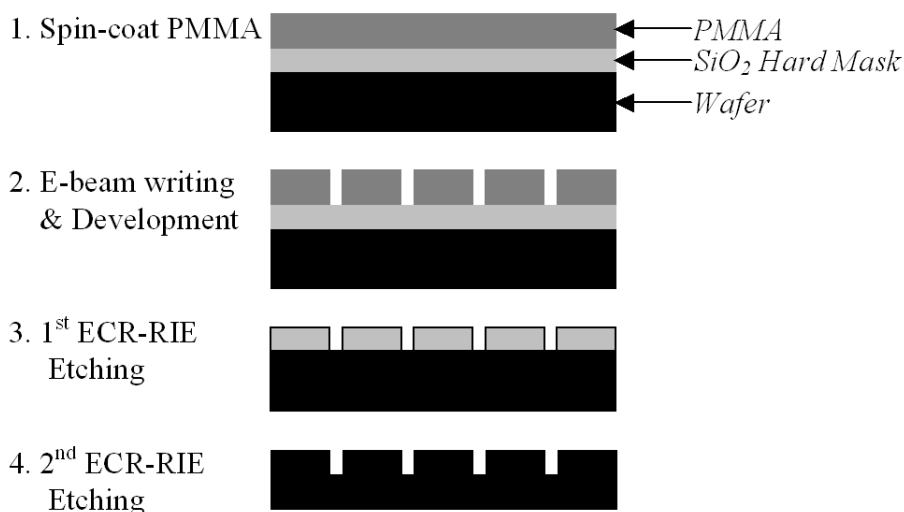


**Figure 8.1** Fabrication procedures of photonic crystal optical components: (1) Spin-coat E-beam resist PMMA on top of the sample; (2) Define photonic crystal patterns into PMMA with E-beam lithography, then remove the exposed area; (3) The patterns are transferred from PMMA to SiO<sub>2</sub> with ECR-RIE etching and the residual PMMA is removed; (4) The patterns are transferred from SiO<sub>2</sub> to the underlying wafer with ECR-RIE etching and the residual SiO<sub>2</sub> hard mask is removed.

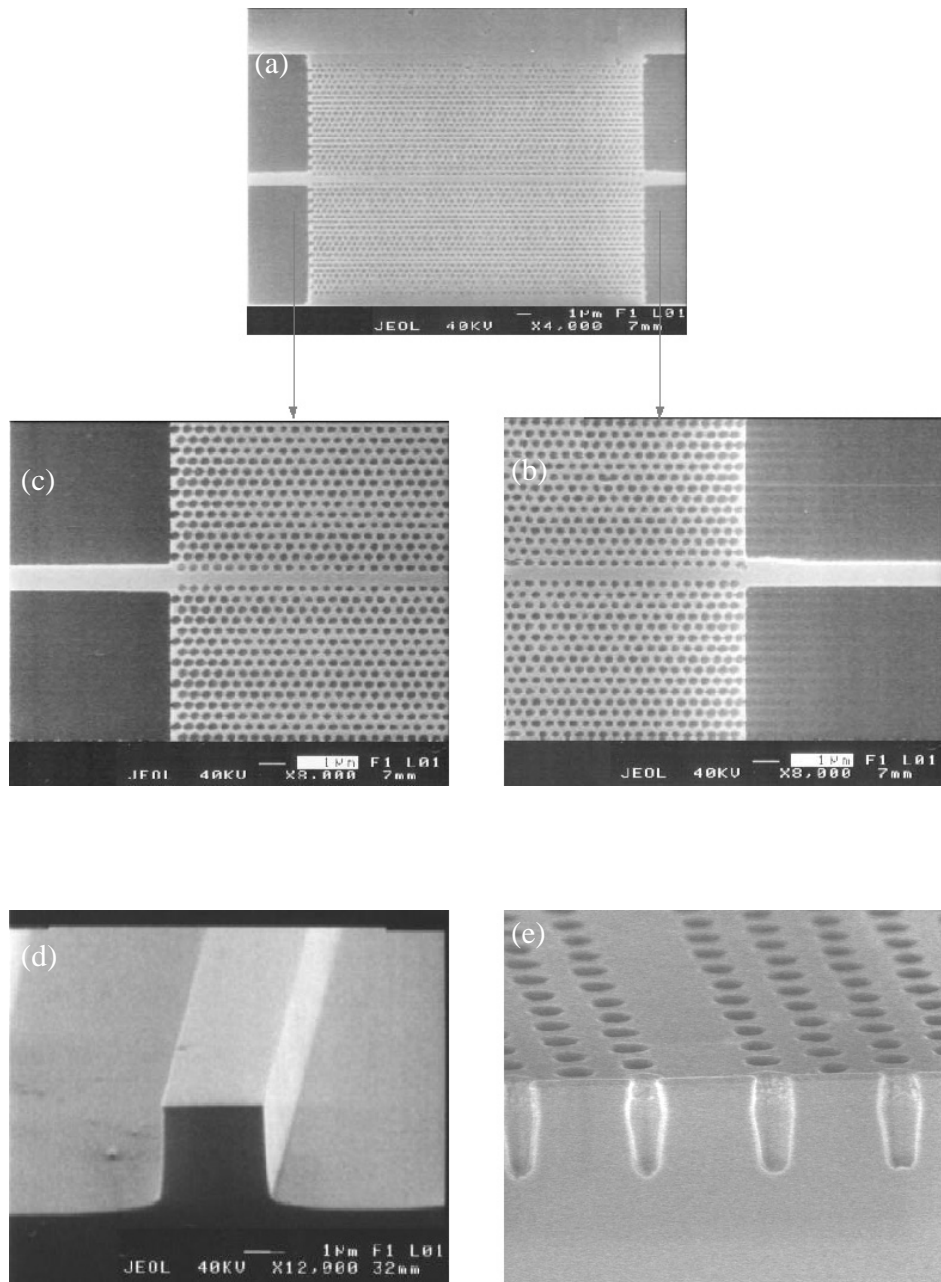


Fig. 8.2 (a) SEM image of the PC waveguide region. (b) Magnified view of the right PC interface with the ridge waveguide. (c) Magnified view of the left PC interface with the ridge waveguide. (d) Cross-sectional view of the ridge. (e) Cross-sectional view of the PC waveguide.

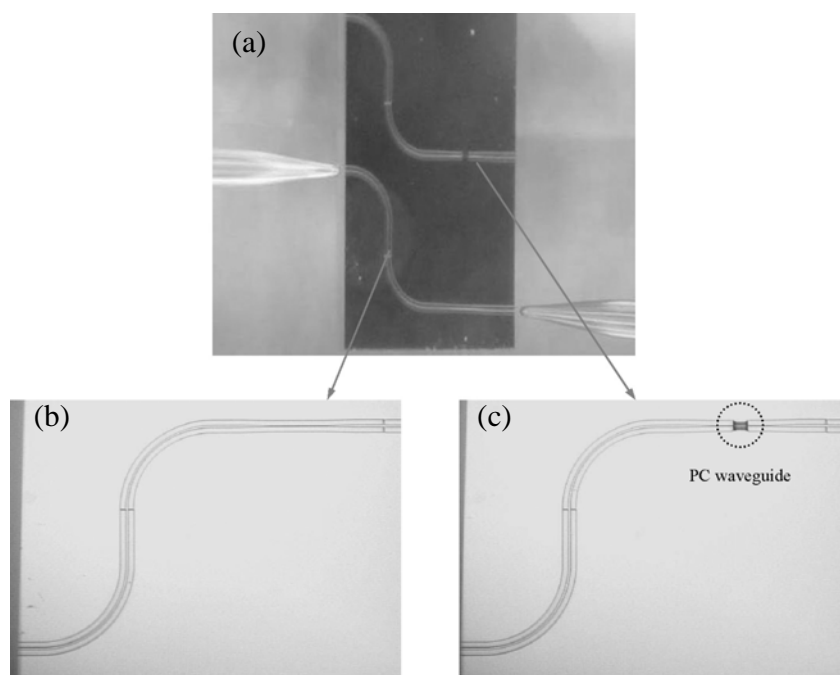


Fig. 8.3 (a) Photograph of the measurement setup: two lensed fibers on either side of the sample are used to couple the light in and out of the waveguides. (b) Magnified view of the S-bend ridge waveguide without the PC section. (c) Magnified view of the S-bend structure with an embedded PC device.

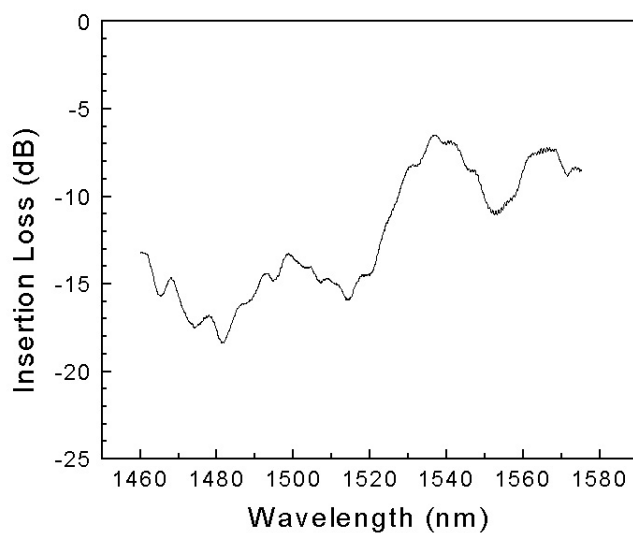


Fig. 8.4 Preliminary measurement result showing the insertion loss of the PC waveguide calibrated against the blank ridge waveguide. The minimum loss is  $\sim -5$  dB around  $\lambda = 1540$  nm.

## CHAPTER 9

# CONCLUDING REMARKS AND FUTURE PERSPECTIVES

In this thesis, several novel optical devices based on photonic crystals, including a MMI based waveguide power splitter, a compact polarizing beam splitter, an intersection of nonidentical optical waveguides, and a single mode coupled resonator optical waveguide, are designed and analyzed. In addition, a new fabrication method based on the combination of a custom-built blue laser writer and the technique of optical holography is developed for the purpose of mass production of useful photonic crystal devices.

For the MMI waveguide power splitter, the device size reduction compared to the conventional MMI power splitter can be attributed to the large dispersion of the photonic crystal waveguides. We also show an example of a compact Mach-Zehnder interferometer based on a MMI splitter and combiner.

For the compact polarizing beam splitter, TE light is confined with the photonic bandgap effect, while TM light is guided through an index-like effect. Due to the different guiding mechanisms, TM and TE light have strikingly different beat lengths, which is utilized to separate the two polarizations in a directional coupler no longer than

24.2 $\mu\text{m}$ . The extinction ratios are found to be around 20dB for both TE and TM polarized light.

In order to build an intersection to accommodate the wide transmission band in the current optical communication systems, two waveguides based on coupled resonators are designed to have different transmission bands without overlap, which enables light in the two corresponding bands to propagate through the intersection with no cross-talk and with excellent transmission. This design is for the purpose of

Optical waveguides with only single mode propagation are important for many applications. For this purpose, we presented a way to design a single mode  $\Gamma$ -K direction coupled-resonator-optical-waveguides in a triangular lattice photonic crystal of air holes in a dielectric material. It is shown that insertion of an extra anisotropic hole along a specific direction in the cavity can lead to single even mode transmission in the whole PBG region.

For the purpose of mass production of functional photonic crystal devices, we demonstrate an approach of relatively rapid fabrication of two-dimensional photonic crystals with embedded defects by combining a custom-built blue-laser-writer and the technique of optical holography. The blue laser writer is used to define various defect patterns first, and then the optical holography is used to create two-dimensional photonic

crystals on the samples with the pre-defined defects. Finally the photonic crystal patterns are transferred into the InP substrates by ECR-RIE etching.

Compared to other approaches, electron-beam lithography still has the most flexibility for fabricating photonic crystal devices. Therefore we developed complete processing procedures by using electron-beam lithography and ECR-RIE dry etching. Some preliminary measurement results for the coupling between conventional ridge waveguides and photonic crystal waveguides are also presented.

## REFERENCES

1. E. Yablonovitch, "Inhibited spontaneous emission in solid-state physics and electronics," *Phys. Rev. Lett.*, vol. 58, no. 20, pp. 2059-2062, May 1987.
2. J. D. Joannopoulos, R. D. Meade, and J. N. Winn, *Photonic Crystals* (Princeton, NJ: Princeton Univ. Press, 1995).
3. S. Fan, P. Villeneuve, and J. D. Joannopoulos, "Channel drop through localized states," *Phys. Rev. Lett.*, vol. 80, pp. 960-963 (1998).
4. S. H. Kim, H. Y. Ryu, H. G. Park, G. H. Kim, Y. S. Khoi, Y. H. Lee, and J. S. Kim, "Two-dimensional photonic crystal hexagonal waveguide ring laser," *Appl. Phys. Lett.*, vol. 81, pp. 2499-2501 (2002).
5. A. Mekis, J. C. Chen, I. Kurland, S. Fan, P. R. Villeneuve, and J. D. Joannopoulos, "High transmission through sharp bends in photonic crystal waveguides," *Phys. Rev. Lett.*, vol. 77, pp. 3787-3790 (1996).
6. K. Hosomi, and T. Katsuyama, "A dispersion compensator using coupled defects in a photonic crystal," *IEEE J. Quantum Electro.*, vol. 38, pp. 825-829 (2002).
7. S. Boscolo, M. Midrio, and C. G. Someda, "Coupling and decoupling of electromagnetic waves in parallel 2-D photonic crystal waveguides," *IEEE J. Quantum Electro.*, vol. 38, pp. 47-53 (2002).
8. S. Fan, S. G. Hohnson, J. D. Joannopoulos, C. Manolatou, and H. A. Haus, "Waveguide branches in photonic crystals," *J. Opt. Soc. Am. B*, vol. 18, pp. 162-165 (2001).
9. S. Y. Lin, E. Chow, V. Hietala, P. R. Villeneuve, and J. D. Joannopoulos, "Experimental demonstration of guiding and bending of electromagnetic waves in a photonic crystal," *Science*, vol. 282, pp. 274-276 (1998).
10. A. Adibi, R. K Lee, Y. Xu, et al., "Design of photonic crystal optical waveguides with singlemode propagation in the photonic bandgap," *Electron. Lett.* vol. 36, pp. 1376-1378 (2000).
11. S. Kim et al., "Ultracompact high-efficiency polarizing beam splitter with a hybrid photonic crystal and conventional waveguide structure," *Opti. Lett.*, vol. 28, pp. 2384-2386, Dec. 2003.

12. T. F. Krauss et al., "Two-dimensional photonic-bandgap structures operating at near-infrared wavelengths," *Nature*, vol. 383, pp. 699–702, 1996.
13. M. Loncar, D. Nedeljkovic, T. Doll, J. Vuckovic, A. Scherer, and T. P. Pearsall, "Waveguiding in planar photonic crystals," *Appl. Phys. Lett.*, vol. 77, No. 13, pp. 1937-1939, 2000.
14. O. Painter, R. K. Lee, A. Scherer, A. Yariv, J. D. O'Brien, P. D. Dapkus, and I. Kim, "Two-Dimensional Photonic Band-Gap Defect Mode Laser," *Science*, Vol. 284, pp. 1819-1821, 1999.
15. E. Chow, S. Y. Lin, S. G. Johnson, P. R. Villeneuve, J. D. Joannopoulos, J. R. Wendt, G. A. Vawter, W. Wubrzycki, H. Hou, and A. Alleman, "Three-dimensional control of light in a two-dimensional photonic crystal slab," *Nature*, Vol. 407, pp. 983-985, 2000.
16. S. Noda, A. Chutinan, and M. Imada, "Trapping and emission of photons by a single defect in a photonic bandgap structure," *Nature*, Vol. 407, pp. 608-610, 2000.
17. L. Pang, W. Nakagawa, and Y. Fainman, "Fabrication of two-dimensional photonic crystals with controlled defects by use of multiple exposures and direct write," *Appl. Opt.*, Vol. 42, NO. 27, pp. 5450-5456, 2003.
18. S. G. Johnson, and J. D. Joannopoulos, "Block-iterative frequency-domain methods for Maxwell's equations in a planewave basis," *Optics Express*, vol. 8, pp. 173-190 (2001).
19. A. Taflove, *Computational Electromagnetics: The Finite-Difference Time-Domain Method* (Artech, Boston, Mass., 1995).
20. D. Zhao, B. Shi, Z. Jiang, Y. Fan, and X. Wang, "Silicon-based optical waveguide polarizer using photonic band gap," *Appl. Phys. Lett.*, vol. 81, pp. 409-411 (2002).
21. J. C. Knight, J. Broeng, T. A. Birks, and P. St. J. Russell, "Photonic band gap guidance in optical fibers," *Science*, vol. 282, pp. 1476-1478 (1998).
22. L. M. Li, "Two-dimensional photonic crystals: candidate for wave plates," *Appl. Phys. Lett.*, vol. 78, pp. 3400-3402 (2001).
23. D. R. Solli, C. F. McCormich, R. Y. Chiao, and J. M. Hickmann, "Experimental demonstration of photonic crystal waveplates," *Appl. Phys. Lett.*, vol. 82, pp. 1036-1038 (2003).

24. J. Yonekura, M. Ikeda, and T. Baba, "Analysis of finite 2-D photonic crystals and lightwave devices using the scattering matrix method," *J. Lightwave Technol.* Vol. 17, pp. 1500-1508 (1999).
25. L. B. Soldano and E. C. M. Pennings, "Optical multi-mode interference devices based on self-imaging: Principles and applications," *J. Lightwave Technol.*, vol. 13, pp. 615-627, Apr. 1995.
26. D. S. Levy, K. H. Park, R. Scarmozzino, R. M. Osgood, Jr., C. Dries, P. Studenkov, and S. Forrest, "Fabricatin of ultracompact 3-dB  $2 \times 2$  MMI power splitters," *IEEE Photon. Technol. Lett.*, vol. 11, pp. 1009-1011, Aug. 1999.
27. M. L. Masanovic, E. J. Skogen, J. S. Barton, J. M. Sullivan, D. J. Blumenthal, and L. A. Coldren, "Multimode interference-based two-stage  $1 \times 2$  light splitter for compact photonic integrated circuits," *IEEE Photon. Technol. Lett.*, vol. 15, pp. 706-708, May 2003.
28. P. Sanchis, J. Garcia, A. Martinez, F. Cuesta, A. Griol, and J. Marti, "Analysis of adiabatic coupling between photonic crystal single-line-defect and coupled-resonator optical waveguides," *Optics Lett.*, vol. 28, pp. 1903-1905 (2003).
29. M. Notomi, A. Shinya, K. Yamada, J. Takahashi, C. Takahashi, and I. Yokohama, "Structural tuning of guiding modes of line-defect waveguides of silicon-on-insulator photonic crystal slabs," *IEEE J. Quantum Electro.*, vol. 38, pp. 736-742 (2002).
30. P. Wei, and W. Wang, "A TE-TM mode splitter on Lithium Niobate using Ti, Ni, and MgO diffusions," *IEEE Photon. Technol. Lett.*, vol. 6, pp. 245-248, Feb. 1994.
31. L. B. Soldano et al., "Mach-Zehnder interferometer polarization splitter in InGaAsP-InP," *IEEE Photon. Technol. Lett.*, vol. 6, pp. 402-405, Mar.1994.
32. J. M. Hong et al., "Design and fabrication of a significantly shortened multimode interference coupler for polarization splitter application," *IEEE Photon. Technol. Lett.*, vol. 15, pp. 72-74, Jan.2003.
33. S. Kim et al., "Ultracompact high-efficiency polarizing beam splitter with a hybrid photonic crystal and conventional waveguide structure," *Opti. Lett.*, vol. 28, pp. 2384-2386, Dec. 2003.
34. A. Adibi et al., "Guiding mechanisms in dielectric-core photonic-crystal optical waveguides," *Phys. Rev. B*, vol. 64, pp. 33308, Jun. 2001.

35. P. I. Borel et al., "Efficient propagation of TM polarized light in photonic crystal components exhibiting band gaps for TE polarized light," *Opt. Express*, vol. 11, pp. 1757-1762, Jul. 2003.
36. R. C. Alferness, and L. L. Buhl, "Low-cross-talk waveguide polarization multiplexer/demultiplexer for  $\lambda=1.32\mu\text{m}$ ," *Opti. Lett.*, vol. 10, pp. 140-142, Apr. 1984.
37. Q. Min, "Effective index method for heterostructure-slab-waveguide-based two-dimensional photonic crystals," *Appl. Phys. Lett.*, vol. 81, pp. 1163-1165, Aug. 2002.
38. H. Benisty et al., "Optical and confinement properties of two-dimensional photonic crystals," *J. Lightwave Technol.*, vol. 17, pp. 2063-2077, Nov. 1999.
39. J. P. Berenger, "A perfectly matched layer for the absorption of electromagnetic waves," *J. Comput. Phys.*, vol. 114, pp. 185-200, Oct. 1994.
40. Y. Sugimoto et al., "Design, fabrication, and characterization of coupling-strength-controlled directional coupler based on two-dimensional photonic-crystal slab waveguides," *Appl. Phys. Lett.*, vol. 83, pp. 3236-3238, Oct. 2003.
41. A. Chutinan, M. Okano, and S. Noda, "Wider bandwidth with high transmission through waveguide bends in two-dimensional photonic crystal slabs," *Appl. Phys. Lett.*, vol. 80, pp. 1698-1700, Mar. 2002.
42. J. Moosburger et al., "Enhanced transmission through photonic-crystal-based bent waveguides by bend engineering," *Appl. Phys. Lett.*, vol. 79, pp. 3579-3581, Nov. 2001.
43. S. Olivier et al., "Improved 60° bend transmission of submicron-width waveguides defined in two-dimensional photonic crystals," *J. Lightwave Technol.*, vol. 7, pp. 1198-1203, Jul. 2002.
44. Tao Liu, Armis R. Zakharian, Mahmoud Fallahi, Jerome V. Moloney, Masud Mansuripur, "Multimode Interference-Based Photonic Crystal Waveguide Power Splitter," *J. Lightwave Tech.*, vol. 22, pp. 2842-2846 (2004).
45. Steven G. Johnson, Christina Manolatos, Shanhui Fan, Pierre R. Villeneuve, and J. D. Joannopoulos, H. A. Haus, "Elimination of cross talk in waveguide intersections," *Optics Lett.*, vol. 23, pp. 1855-1857 (1998).
46. Sheng Lan, and Hiroshi Ishikawa, "Broadband waveguide intersections with low cross talk in photonic crystal circuits," *Optics Lett.*, vol. 27, pp. 1567-1569 (2002).

47. Young-Geun Roh, Sungjoon Yoon, Heonsu Jeona, Seung-Ho Han and Q-Han Park, "Experimental verification of cross talk reduction in photonic crystal waveguide crossings," *Appl. Phys. Lett.*, vol. 85, pp. 3351-3353 (2004).
48. N. Stefanou, and A. Modinos, "Impurity bands in photonic insulators," *Phys. Rev. B*, vol. 57, no. 19, pp. 12,127-12,133 (1998).
49. A. Yariv, Y. Xu, R. K. Lee, and A. Scherer, "Coupled-resonator optical waveguide: a proposal and analysis," *Optics Lett.*, vol. 24, no. 11, pp. 711-713, (1999).
50. Mohammad Soltani, Ali Adibi, Yong Xu, Reginald K. Lee, "Systematic design of single-mode coupled-resonator optical waveguides in photonic crystals", *Optics Lett.*, vol. 28, no. 20, pp. 1978-1980 (2003).
51. A. Melloni, F. Morichetti, and M. Martinelli, "Optical slow wave structures," *Optics and Photonics News*, vol. 14, no. 11, pp. 44-48, Nov. 2003.
52. S. Mingaleev, and Y. Kivshar, "Nonlinear transmission and light localization in photonic-crystal waveguides," *J. Opt. Soc. Am. B*, vol. 19, no. 9, pp. 2241-2249, Sep. 2002.
53. M. Dinu, R. L. Willett, K. Baldwin, L. N. Pfeiffer, and K. W. West, "Waveguide tapers and waveguide bends in AlGaAs-based two-dimensional photonic crystals," *Appl. Phys. Lett.*, vol. 83, no. 22, pp. 4471-4473, Dec. 2003.
54. Y. Akahane, T. Asano, B. S. Song, and Susumu Noda, "Investigation of high-Q channel drop filters using donor-type defects in two-dimensional photonic crystal slabs," *Appl. Phys. Lett.*, vol. 83, no. 8, pp. 1512-1514, Aug. 2003.
55. L. C. Andreani, and M. Agio, "Intrinsic diffraction losses in photonic crystal waveguides with line defects," *Appl. Phys. Lett.*, vol. 82, no. 13, pp. 2011-2013, Mar. 2003.
56. L. Pang, W. Nakagawa, and Y. Fainman, "Fabrication of two-dimensional photonic crystals with controlled defects by use of multiple exposures and direct write," *Appl. Opt.*, Vol. 42, NO. 27, pp. 5450-5456, 2003.
57. X. Checoury, P. Boucaud, J.M. Lourtioz, O. Gauthier-Lafaye, S. Bonnefont, D. Mulin, J. Valentin, F. Lozes-Dupuy, F. Pommereau, C. Cuisin, E. Derouin, O. Drisse, L. Legouezigou, F. Lelarge, F. Poingt, G. H. Duan, and A. Talneau, "1.5 mm room-temperature emission of square-lattice photonic-crystal waveguide lasers with a single line defect," *Appl. Phys. Lett.*, vol. 86, 151111, Apr. 2005.